THE ASTROPHYSICAL JOURNAL SUPPLEMENT SERIES, 78:341–364, 1992 February

A HYDRODYNAMIC APPROACH TO COSMOLOGY: METHODOLOGY

RENYUE CEN
Princeton University Observatory, Princeton University, Princeton, NJ 08544
Received 1990 November 5; accepted 1991 July 2

ABSTRACT

An accurate and efficient hydrodynamic code for evolving self-gravitating cosmological systems is described. The code may be coupled with a standard particle code, e.g., a particle-mesh code, if point-mass collisionless components are needed in the model. The hydrodynamic code is a flux-based mesh code originally designed for engineering hydrodynamical applications. A variety of checks have been made which indicate that the resolution of the code is a few cells, giving accuracy for integral energy quantities in our simulations of 1%–3% over the whole runs. The advantages of using a true hydrodynamic code over an N-body code are manifold, since the observed universe is baryonic, and its early evolution should be treated via the classic Euler equations of hydrodynamics. In addition, the distribution of baryonic matter in temperature and density and the background radiation fields can be directly obtained, enabling comparison between these distributions and astronomical observations. A standard particle-mesh code is also described, for the reason that we will use it when pointlike components are introduced. We track separately six species (e^-, H I, H II, He I, He II, He III), computing in detail (non–LTE) relevant ionization and recombination processes, as well as line and continuum heating and cooling. The background radiation field is simultaneously determined in the range 1 eV to 100 keV allowing, in a spatially averaged fashion, for absorption, emission, and cosmological effects. We show how the inevitable numerical inaccuracies can be estimated and to some extent overcome. For example, the mean Zel'dovich-Sunyaev y-parameter is calculated to be 6.0×10^{-6} in a simulation with 128^3 dark matter particles and 128^3 cells, a maximum scale size of $L = 64h^{-1}$ Mpc, and a minimum wavelength of $\lambda_{\rm min} = 1h^{-1}$ Mpc, with $h = 0.5$ and $b = 1.0$. By comparing the results of runs with different values of (N, $L_{\rm max}$, $L_{\rm min}$), we extrapolate to $y = (1.25 \pm 0.65) \times 10^{-5}$ as (N^{-1}, $L_{\rm max}^{-1}$, $L_{\rm min}$) $\rightarrow 0$.

Subject headings: cosmology: theory — dark matter — hydrodynamics — methods: numerical

1. INTRODUCTION

The observed universe is baryonic, and, since it evolved from conditions close to those idealized by a smooth gaseous flow in the standard cosmological scenario from the hot big bang, its description and evolution in the first instance should be treated via the classic Euler equations of hydrodynamics. In addition, there may also exist a dark matter component of the universe described by the Vlasov or collisionless Boltzmann equations. Besides, at later times when stars or galaxies formed, they are also better treated as collisionless particles, although they may feed back energy in various forms, such as supernovae, galactic winds, quasar output, etc. The latter collisionless component is best treated by codes such as the particle-mesh (PM) code, the particle-particle-particle-mesh (PPPM) code or tree code, which, historically, can be traced back to N-body codes familiar from treatments of interacting mass points in Newtonian mechanics (for an excellent review cf. White 1988). To date, most work in this field has utilized mathematical techniques appropriate for a collisionless (dark matter) fluid. Direct N-body (Aarseth 1971, 1974) simulations are severely limited by the number of particles, owing to the fact that computer time is proportional to N^k ($k \geq 2$), $N \sim 10^{4.5}$ is about the maximum number of particles; PM and PPPM codes (Efstathiou et al. 1985; Melott & Fry 1986) are able to include about 10^6 or even more particles, for they use grids to calculate the gravitational forces, and computer time is proportional to $N \log N$; a tree code (Bouchet & Hernquist 1988; Hernquist & Katz 1989) has similar properties. In fact, the N-body, collisionless approach is valid if very large scales are to be treated. This can be understood simply. The maximum likely temperature for the local intergalactic medium (IGM) of 10^8 K (matching the temperature of the X-ray emitting gas of rich clusters) corresponds to a sound speed of 10^3 km s^{-1} or a communication distance of 10 Mpc in a Hubble time. Thus it is difficult, in any cosmological scenario, for pressure forces to be significant in moving matter on scales very much greater than 10 Mpc, and thus, on large scales, pressure forces are unimportant. Another way to understand this is the following: it appears that the cluster scale of $\sim$5 Mpc has just left the linear density perturbation regime at present (cf. Davis & Peebles 1983), so on scales very much greater than 5 Mpc, matter has not been shocked; then the proper peculiar internal energy on these scales should be small compared with proper peculiar kinetic energy. If nonlinear structures exist on scales very much greater than 100 Mpc (cf. Tully 1982; Broadhurst et al. 1990), we expect that an N-body approach to understanding them (cf. Park 1990) is the best.

The motivation to take a hydrodynamic approach is, however, very strong. First, and most important, thermodynamic variables become accessible, with the consequence that it becomes possible to compute other new physical diagnostics. For example, the availability of [$T(\mathbf{r})$, $P(\mathbf{r})$] allows the determination of radiative emission in UV and X-ray bands to be compared with the observed (or required) background radiation fields. In addition, $\int P\, dl$ is proportional to the distortion of the cosmic background radiation (CBR) spectrum along a given line of sight resulting from the Zel'dovich-Sunyaev (1970 and references therein) effect.

The pressure distribution within the IGM is also, in principle, directly determinable from studies of the Lyα clouds seen in absorption spectra of distant quasars (cf. Young et al. 1981; Sargent, Young, & Schneider 1982; Ikeuchi & Ostriker 1986; McGill 1990). This enables various cosmological scenarios to be tested in new ways. Take two popular scenarios, cold dark matter (CDM) and hot dark matter (HDM) as examples. The "bottom-up" hierarchically clustering characteristics of the CDM scenario make heating and cooling processes effective much earlier and perhaps much more important than in the "top-down" fragmenting HDM scenario. The reason is that almost all the cooling processes are quadratic functions of density, and are therefore proportional to $(1 + z)^6$, except for Compton cooling, which is proportional to $(1 + z)^4$, and structure develops earlier in CDM than in HDM models. Quite different consequences for the two scenarios are likely to occur. Until now, tests of theories have been based on the derived density and velocity fields of galaxies which are compared with local measurements. But these are subject to the uncertainty of how well the test objects trace the underlying mass distribution, i.e., the question of "bias." One can expect that new tests will encourage new observations and also constrain the theoretical possibilities more severely than has been hitherto possible.

Second, galaxies and clusters of galaxies, which are the largest gravitationally bound systems discovered so far, both have scales less than 5 Mpc, so pressure is relevant; the physics is really different on these smaller scales from that described by a collisionless fluid. Shocks prevent converging streams of matter from passing through one another, in which process entropy will be produced and the motion of matter will be quite different from that resulting if matter is treated as collisionless particles; for example, when a caustic forms, the perpendicular velocity will be transferred to parallel velocities in part. Radiative emission processes or interaction with the CBR cause energy losses to the gas (cf. Rees & Ostriker 1977; Silk 1977; Binney 1977), which can overwhelm shock heating on scales $\Delta l < 0.1$ Mpc. These processes must play an essential role on these scales, eventually leading to formation of galaxies, globular star clusters, massive stars, etc. Thermonuclear input from young galaxies (Schwarz, Ostriker, & Yahil 1975; Ostriker & Cowie 1981) or gravitationally released energy emitted by quasars (Ikeuchi 1981) can move matter significantly on scales $\Delta l < 5$ Mpc.

Third, because of various situations in different regions, e.g., different density, temperature, etc., the ionization states of hydrogen and helium will be quite different from place to place. The distribution of these species will be very useful to studies of phenomena such as Lyα clouds and the Gunn-Peterson (1965) test.

Finally, there are the higher order processes based on the interaction of matter fluctuations with the radiation produced by the above processes. Examples are expanding H II regions (Rees 1985, 1988) or "mock gravity" (Hogan 1989).

The difficulty in applying hydrodynamics to cosmology has been primarily practical. The available computer hardware and software simply did not allow one to make simulations which simultaneously treated scales $\Delta l_{\rm min} \leq 0.1$ Mpc, at which cooling is most important, and scales $\Delta l_{\rm max} \geq 10$ Mpc, where the thermal input from gravitationally induced shocks is maximal. Work has been done by Melott & Fry (1986), Carlberg & Couchman (1989), and others with "soft particle" or "sticky particle" codes intended to roughly simulate hydrodynamic effects, and Evrard (1988) and Hernquist & Katz (1989) use smooth-particle hydrodynamics (SPH) to mimic the real hydrodynamic effects, but the assignment of hydrodynamic quantities to the particles is somewhat ad hoc in these schemes. The SPH algorithms converge to continuum hydrodynamical solutions when the number of simulated particles increases, but the current computer technology does not allow the necessary minimum number of particles to be employed in cosmological applications to cover the relevant, interesting dynamic range. Chiang, Ryu, & Vishniac (1989) and Ryu, Vishniac, & Chiang (1990) have developed a true hydrodynamical code applied to the cosmological questions, but with a resolution of $10^{4.5}$ cells, which is probably not adequate to span the necessary physical scales. Besides, in all the above codes, cooling and heating processes may not have been included properly and accurately according to our preliminary work on the cooling processes. Adoption of a "cooling curve" is inaccurate; a non–LTE approach is needed. What is required at a minimum is $(\Delta l_{\rm max}/\Delta l_{\rm min})^3 \geq 10^6$ cells with several species followed in each cell. With the fast development in the computer hardware field, it becomes practical now to make simulations with 10^6 cells or even more. Therefore, it is becoming meaningful to have a code available to make full use of the presently available computers.

This paper presents one approach to achieving an efficient and accurate real hydrodynamic code. An efficient hydrodynamic code must satisfy the following requirements: (1) it must have the capability to simulate the main features of the flow, such as shocks and vortex sheets; (2) it must be able to evaluate the effects of viscous terms; (3) the numerical method must be robust, not liable to fail when models are varied; (4) it must be able to handle high-contrast quantities, such as density, pressure, and temperature; and (5) there must be efficiency in both computational and human effort.

This is a formidable list that poses a severe challenge to numerical simulators. Nevertheless, the code we present here appears to have the above characteristics. The code is able to capture a clean shock with about 3–4 cells; viscous diffusive effects are only important when shocks occur, i.e., nonshocking linear regions are unaffected; the code can basically handle what we have wanted to model, though computer costs for various models may vary; rms fluctuations of density, pressure and temperature of 100 in units of their corresponding means are able to be handled, leading to a range of density of 10^7, a range of temperature of 10^9, and a range of pressure of up to 10^{16}; the code is well organized and structured, so it can be maintained at a reasonable effort; besides, the code uses a minimum amount of computer memory and has reasonably high speed. In addition, the code demonstrates very good accuracy. For a simulation with $64 \times 64 \times 64$ cells, the code gives accuracy for integral energy quantities of 1%–3%. A preliminary discussion of both the code and results has been presented in Cen et al. (1990). In § 2 we describe the equations which the code integrates and how we obtained these equations. Section 3 presents the numerical techniques employed. Section 4 describes the method with which we set up initial conditions of simulations. Section 5 demonstrates the tests we have made of the code. Section 6 concludes the paper with some discussion of the significance of the work and directions for further improvements.

2. EQUATIONS

There are two sets of equations, one for the baryonic fluid and the other for collisionless components.

2.1. *Hydrodynamic Equations*

We first present hydrodynamic equations. In comoving coordinates, without any viscous term, the mass conservation equation has the following form (cf. Peebles 1980):

$$\frac{\partial \rho}{\partial t} + \frac{1}{a}\frac{\partial}{\partial x_k}(\rho u_k) = 0 , \tag{1}$$

in the absence of force fields (such as the gravitational field), the momentum equation has the form

$$\frac{\partial \rho u_i}{\partial t} + \frac{1}{a}\frac{\partial}{\partial x_k}(\rho u_i u_k + P\delta_{ik}) = -\frac{\dot{a}}{a}\rho u_i , \tag{2}$$

in the absence of heat conduction, heat source or loss term, or force fields, the energy conservation equation is

$$\frac{\partial E}{\partial t} + \frac{1}{a}\frac{\partial}{\partial x_k}[(E + P)u_k] = -\frac{2\dot{a}}{a}E . \tag{3}$$

Here t is the cosmic time; ρ is the comoving density, which is the product of proper density and a^3; u_k is the proper peculiar velocity; P is the comoving pressure, which is the product of proper pressure and a^3; E is the total peculiar energy (kinetic plus internal energy) per unit comoving volume, defined as $E \equiv P/(\gamma - 1) + \frac{1}{2}\rho u_k^2$; a is the expansion scale factor [$\equiv 1/(1 + z)$, where z is the redshift]; $\dot{a}$ is the derivative of a with respect to time. The terms on the right-hand side of equations (2) and (3) are simply due to the expansion of the universe. In equation (3) we have implicitly assumed that the ratio of the specific heats of the baryonic fluid is $\gamma = \frac{5}{3}$.

Before any real models can be computed, we must include several additional terms in the above three equations and add more equations. There are four terms to be added to the equations:

1. The gravitational source term in the comoving coordinates.
2. The Compton cooling (or heating) term due to interactions of free electrons with the diffuse microwave background radiation field and the diffuse X-ray background radiation field.
3. The integrated radiative cooling-heating term due to hydrogen and helium, which includes electron bremsstrahlung cooling, hydrogen and helium recombination cooling, helium dielectronic recombination cooling, hydrogen and helium collisional ionization cooling, hydrogen and helium collisional excitation cooling, and photoionization heating.
4. Numerical diffusion terms and terms induced from them.

In addition there are five more equations needed: three for evolution of neutral hydrogen (H I), neutral helium (He I) and singly ionized helium (He II) species, an equation of state, and an equation for the evolution of the diffuse background radiation field. After including these terms and equations, the following set of equations is obtained:

$$\frac{\partial \rho}{\partial t} + \frac{1}{a}\frac{\partial}{\partial x_k}(\rho u_k - D_{\rho k}) = 0 , \tag{4a}$$

$$\frac{\partial \rho_{\rm H\,I}}{\partial t} + \frac{1}{a}\frac{\partial}{\partial x_k}(\rho_{\rm H\,I} u_k - D_{\rho_{\rm H\,I} k}) = n(e)(f_{\rm H}\rho - \rho_{\rm H\,I})\alpha_{\rm H\,II}(T) - n(e)\rho_{\rm H\,I}\beta_{\rm H}(T) - \rho_{\rm H\,I}\int_{\nu_0({\rm H})}^{\infty} 4\pi\sigma_\nu({\rm H})\frac{i(\nu)}{h\nu}\,d\nu , \tag{4b}$$

$$\frac{\partial \rho_{\rm He\,I}}{\partial t} + \frac{1}{a}\frac{\partial}{\partial x_k}(\rho_{\rm He\,I} u_k - D_{\rho_{\rm He\,I} k}) = n(e)\rho_{\rm He\,II}[\alpha_{\rm He\,II}(T) + \xi_{\rm He\,II}(T)] - n(e)\rho_{\rm He\,I}\beta_{\rm He\,I}(T) - \rho_{\rm He\,I}\int_{\nu_0({\rm He\,I})}^{\infty} 4\pi\sigma_\nu({\rm He\,I})\frac{i(\nu)}{h\nu}\,d\nu , \tag{4c}$$

$$\frac{\partial \rho_{\rm He\,II}}{\partial t} + \frac{1}{a}\frac{\partial}{\partial x_k}[\rho_{\rm He\,II} u_k - D_{\rho_{\rm He\,II} k}] = n(e)[(1 - f_{\rm H})\rho - \rho_{\rm He\,I} - \rho_{\rm He\,II}]\alpha_{\rm He\,III}(T) - n(e)\rho_{\rm He\,II}\beta_{\rm He\,II}(T) - \rho_{\rm He\,II}\int_{\nu_0({\rm He\,II})}^{\infty} 4\pi\sigma_\nu({\rm He\,II})\frac{i(\nu)}{h\nu}\,d\nu - n(e)\rho_{\rm He\,II}[\alpha_{\rm He\,II}(T) + \xi_{\rm He\,II}(T)] + n(e)\rho_{\rm He\,I}\beta_{\rm He\,I}(T) + \rho_{\rm He\,I}\int_{\nu_0({\rm He\,I})}^{\infty} 4\pi\sigma_\nu({\rm He\,I})\frac{i(\nu)}{h\nu}\,d\nu , \tag{4d}$$

$$\frac{\partial \rho u_i}{\partial t} + \frac{1}{a}\frac{\partial}{\partial x_k}(\rho u_i u_k + P\delta_{ik} - D_{ik}) = -\frac{\dot{a}}{a}\rho u_i - \frac{1}{a}\rho\frac{\partial \phi}{\partial x_i} + \frac{1}{a}\frac{u_i}{u^2}D_{\rho k}\frac{\partial \phi}{\partial x_k}, \tag{5}$$

$$\frac{\partial E}{\partial t} + \frac{1}{a}\frac{\partial}{\partial x_k}[(E+P)u_k - D_{Ek}] = -\frac{2\dot{a}}{a}E - \frac{1}{a}\rho u_k\frac{\partial \phi}{\partial x_k} + \frac{1}{a}D_{\rho k}\frac{\partial \phi}{\partial x_k} - \Lambda_{\rm net}, \tag{6}$$

$$\frac{\partial i(\nu)}{\partial t} = \frac{\dot{a}}{a}\left[\nu\frac{\partial i(\nu)}{\partial \nu} - 3i(\nu)\right] + c[j_{\rm ff}(\nu) + j_{\rm fb,H\ II} + j_{\rm fb,He\ II} + j_{\rm fb,He\ III} - \kappa(\nu)i(\nu)], \tag{7}$$

$$P = \frac{1}{m_P}\left(\rho_{\rm H\ I} + \rho_{\rm H\ II} + \frac{\rho_{\rm He\ I} + \rho_{\rm He\ II} + \rho_{\rm He\ III}}{4} + \rho_{\rm H\ II} + \frac{\rho_{\rm He\ II}}{4} + \frac{\rho_{\rm He\ III}}{2}\right)kT, \tag{8}$$

where $\alpha_{\rm H\ II}(T)$ is the H II recombination coefficient; $\alpha_{\rm He\ II}(T)$ is the He II recombination coefficient; $\alpha_{\rm He\ III}(T)$ is the He III recombination coefficient; $\beta_{\rm H}(T)$ is the H I collisional ionization coefficient; $\beta_{\rm He\ I}(T)$ is the He I collisional ionization coefficient; $\beta_{\rm He\ II}(T)$ is the He II collisional ionization coefficient; $\kappa(\nu)$ is the mean absorption coefficient due to both hydrogen and helium gas (see also eq. [38]); $\Lambda_{\rm net}$ is the net cooling term; ν_0(H) is the H I ionization energy; ν is the radiation frequency; ν_0(He I) is the He I ionization energy; ν_0(He II) is the He II ionization energy; $\rho_{\rm H\ I}$ is the comoving density of netural hydrogen (H I); $\rho_{\rm He\ I}$ is the comoving density of neutral helium (He I); $\rho_{\rm He\ II}$ is the comoving density of singly ionized helium (He II); σ_ν(H) is the hydrogen photoionization cross section; σ_ν(He I) is the He I photoionization cross section; σ_ν(He II) is the He II photoionization cross section; $f_{\rm H}$ is the mass fraction of hydrogen, which we take as 0.76; $f_{\rm He}$ is the mass fraction of helium, which we take as 0.24; $i(\nu)$ is the intensity of the diffuse background radiation field; $j_{\rm ff}(\nu)$ is the emissivity of the baryon gas due to the bremsstrahlung radiation process (see also eq. [39]); $j_{\rm fb,H\ II}(\nu)$, $j_{\rm fb,He\ II}(\nu)$, $j_{\rm fb,He\ III}(\nu)$ are the emissivity of the free-bound processes due to H II, He II, and He III, respectively (see eqs. [40a]–[40c]); $n(e)$ is the electron number density in units of cm^{-3}; $\xi_{\rm H\ II}(T)$ is the H II dielectric recombination coefficient. The third term on the right-hand side of equation (5) and the third term on the right-hand side of equation (6) are due to the fact that the density diffusion term in the gravitational field does work against this field. We have, at present, maintained the electrons and ions at the same temperature. It would be a minor and perhaps necessary modification to allow for separate ion/electron temperatures. Equation (7) determines the evolution of the mean intensity $i(\nu)$ as affected by cosmic expansion (terms linear in $\dot{a}/a$) and sources $j(\nu)$ and sinks $\kappa(\nu)$ of radiation. For the forms of diffusion terms $D_{\rho k}$, $D_{\rho_{\rm H\ I}k}$, $D_{\rho_{\rm He\ I}k}$, $D_{\rho_{\rm He\ II}k}$, D_{ik}, D_{Ek} (see eqs. [11a]–[11c]).

Equation (6) is derived from equation (4a) and equation (5) plus the first law of thermodynamics. In the comoving coordinates of the expanding universe in the presence of numerical dissipation, the heat input per unit volume can then be shown to be

$$\frac{dQ}{dt} = \frac{1}{a}\rho\left[F_1\left(\frac{\partial u_i}{\partial x_1}\right)^2 + F_2\left(\frac{\partial u_i}{\partial x_2}\right)^2 + F_3\left(\frac{\partial u_i}{\partial x_3}\right)^2\right] - \Lambda_{\rm net}. \tag{9}$$

The "extra" terms on the right-hand sides of equations (4) and (5) were designed so that equation (9) has the form it does. Entropy generation must be Galilean-invariant and independent of the gravitational potential. The numerical diffusion terms in equations (4), (5), (6), and (9) are defined as

$$F_k \equiv {\rm VIS}_2(C + |u_k|)(\Delta l)^3\frac{1}{4P}\frac{\partial^2 P}{\partial x_k^2} \qquad (k = 1, 2, 3), \tag{10}$$

$$D_{\rho k} \equiv F_k\frac{\partial \rho}{\partial x_k}, \quad D_{\rho_{\rm H\ I}k} \equiv F_k\frac{\partial \rho_{\rm H\ I}}{\partial x_k} \qquad (k = 1, 2, 3), \tag{11a}$$

$$D_{\rho_{\rm He\ I}k} \equiv F_k\frac{\partial \rho_{\rm He\ I}}{\partial x_k}, \quad D_{\rho_{\rm He\ II}k} \equiv F_k\frac{\partial \rho_{\rm He\ II}}{\partial x_k} \qquad (k = 1, 2, 3), \tag{11b}$$

$$D_{ik} \equiv F_k\frac{\partial \rho u_i}{\partial x_k}, \quad D_{Ek} \equiv F_k\frac{\partial E}{\partial x_k} \qquad (k = 1, 2, 3), \tag{11c}$$

where x_1, x_2, and x_3 are three coordinates of comoving positions; u_1, u_2, and u_3 are three components of the proper peculiar velocities; F_1, F_2, and F_3 are three numerical diffusion parameters, which are functions of local pressure, second derivatives of pressure, density, and velocity (eq. [10]); C is the local speed of sound; Δl is cell size; ${\rm VIS}_2$ is the input viscosity parameter, which we take to have a value near unity.

For the primordial baryonic matter, which consists of only hydrogen and helium, the following cooling or heating rates (in units of ergs cm^{-3} s^{-1}), due to radiative processes and interaction between radiation and matter, are relevant. The bremsstrahlung radiation coefficient and photoionization cross sections are taken from Osterbrock (1989). The Compton cooling formula is taken

from Peebles (1971, p. 202). The H II and He III recombination coefficients are taken from Spitzer (1978). The rest of the collisional excitation, collisional ionization, and recombination coefficients are taken from Black (1981), but for the coefficients of processes involving a free electron and an orbital electron, we multiply them by $(1 + T_5^{1/2})^{-1}$ to take account of the fact that these cross sections go as $T^{-1/2}$ when temperature $T \geq 10^5$.

2.1.1. *Cooling Process Rates* (in ergs cm^{-3} s^{-1})

1. Collisional ionization cooling:

i) H:

$$\zeta_{\rm H}(T) = 1.27 \times 10^{-21} T^{1/2}(1 + T_5^{1/2})^{-1} e^{-157809.1/T} n(e) n({\rm H}), \tag{12a}$$

ii) He:

$$\zeta_{\rm He}(T) = 9.38 \times 10^{-22} T^{1/2}(1 + T_5^{1/2})^{-1} e^{-285335.4/T} n(e) n({\rm He}), \tag{12b}$$

iii) He II:

$$\zeta_{\rm He\,II}(T) = 4.95 \times 10^{-22} T^{1/2}(1 + T_5^{1/2})^{-1} e^{-631515/T} n(e) n({\rm He\,II}), \tag{12c}$$

iv) He($2\,^3S$):

$$\zeta_{{\rm He}(2\,^3S)}(T) = 5.01 \times 10^{-27} T^{-0.1687}(1 + T_5^{1/2})^{-1} e^{-55338/T} n(e)^2 n({\rm He\,II}). \tag{12d}$$

2. Recombination cooling:

i) H II:

$$\eta_{\rm H}(T) = 8.70 \times 10^{-27} T^{1/2} \left(\frac{T}{10^3}\right)^{-0.2} \Big/ \left[1 + \left(\frac{T}{10^6}\right)^{0.7}\right] n(e) n({\rm H\,II}), \tag{13a}$$

ii) He II:

$$\eta_{\rm He}(T) = 1.55 \times 10^{-26} T^{0.3647} n(e) n({\rm He\,II}), \tag{13b}$$

iii) He III:

$$\eta_{\rm He\,III}(T) = 3.48 \times 10^{-26} T^{1/2} \left(\frac{T}{10^3}\right)^{-0.2} \Big/ \left[1 + \left(\frac{T}{10^6}\right)^{0.7}\right] n(e) n({\rm He\,III}). \tag{13c}$$

3. Dielectronic recombination cooling (He):

$$\omega_{\rm He\,II}(T) = 1.24 \times 10^{-13} T^{-1.5} e^{-470000/T}(1 + 0.3 e^{-94000/T}) n(e) n({\rm He\,II}). \tag{14}$$

4. Collisional excitation cooling:

i) H (all n):

$$\psi_{\rm H}(T) = 7.5 \times 10^{-19}(1 + T_5^{1/2})^{-1} e^{-118348/T} n(e) n({\rm H}), \tag{15a}$$

ii) He II ($n = 2$):

$$\psi_{\rm He\,II}(T) = 5.54 \times 10^{-17} T^{-0.397}(1 + T_5^{1/2})^{-1} e^{-473638/T} n(e) n({\rm He\,II}), \tag{15b}$$

iii) He I ($n = 2, 3, 4$ triplets):

$$\psi_{\rm He}(T) = 9.10 \times 10^{-27} T^{-0.1687}(1 + T_5^{1/2})^{-1} e^{-13179/T} n(e)^2 n({\rm He\,II}). \tag{15c}$$

5. Bremsstrahlung cooling of all ions:

$$\theta(T) = 1.42 \times 10^{-27} g_{\rm ff} T^{1/2}[n({\rm H\,II}) + n({\rm He\,II}) + 4n({\rm He\,III})] n(e). \tag{16}$$

6. Compton cooling:

i) Due to microwave background radiation field:

$$\frac{du}{dt} = -\frac{8}{3}\frac{\sigma_{es}}{m_e c}\left[\frac{n(e)}{n_{tot}}\right]\left(1 - \frac{T_r}{T}\right)\epsilon_r u \,, \tag{17}$$

ii) Due to the diffuse X-ray background radiation field:

$$\frac{du}{dt} = -\frac{8}{3}\frac{\sigma_{es}}{m_e c}\left[\frac{n(e)}{n_{tot}}\right]\left(1 - \frac{T_x}{T}\right)\epsilon_x u \,, \tag{18}$$

where T_x is the effective radiation temperature of the diffuse X-ray background radiation field in kelvins, which is defined as

$$T_x \equiv \frac{1}{4k}\frac{\int i(\nu) h\nu \, d\nu}{\int i(\nu) d\nu} \,, \tag{19}$$

where $i(\nu)$ is the radiation intensity of the X-ray field, ν is the frequency, k is Boltzmann's constant, h is Planck's constant, $\sigma_{es} = 0.665 \times 10^{-24}$ cm^2 is the Thomson cross section, m_e is the electron mass, c is the speed of light, ϵ_r is the radiation energy density, u is the baryonic matter internal energy density, T_r is the CBR radiation temperature in kelvins, T is the baryonic matter temperature in kelvins, $T_5 \equiv T/10^5$, $n(e)$ is the electron number density, n_{tot} is the total number density of baryonic matter, and g_{ff} is the Gaunt factor, which is taken to be 1.5.

2.1.2. *Heating Process Rates*

1. Photoionization heating:

i) H I:

$$n(\mathrm{H}) \int_{\nu_0(\mathrm{H})}^{\infty} 4\pi\sigma_\nu(\mathrm{H}) \frac{i(\nu)}{h\nu} [h\nu - h\nu_0(\mathrm{H})] d\nu \,, \tag{20}$$

ii) He I:

$$n(\mathrm{He}) \int_{\nu_0(\mathrm{He})}^{\infty} 4\pi\sigma_\nu(\mathrm{He}) \frac{i(\nu)}{h\nu} [h\nu - h\nu_0(\mathrm{He})] d\nu \,, \tag{21}$$

iii) He II:

$$n(\mathrm{He\ II}) \int_{\nu_0(\mathrm{He\ II})}^{\infty} 4\pi\sigma_\nu(\mathrm{He\ II}) \frac{i(\nu)}{h\nu} [h\nu - h\nu_0(\mathrm{He\ II})] d\nu \,, \tag{22}$$

where the cross sections have the forms

i) H:

$$\sigma_\nu(\mathrm{H}) = 1.18 \times 10^{-11} \nu^{-4} \frac{e^{-4(\arctan \epsilon_1)/\epsilon_1}}{1 - e^{-2\pi/\epsilon_1}} \qquad \text{for } \nu \geq \nu_0(\mathrm{H}) \tag{23}$$

and zero otherwise, where $\epsilon_1 = [\nu/\nu_0(\mathrm{H}) - 1]^{1/2}$ and $\nu_0(\mathrm{H})$ is the hydrogen ionization energy in units of eV.

ii) He:

$$\sigma_\nu(\mathrm{He}) = 1.13 \times 10^{-14}\left(\frac{1}{\nu^{2.05}} - \frac{9.775}{\nu^{3.05}}\right) \qquad \text{for } \nu \geq \nu_0(\mathrm{He}) \tag{24}$$

and zero otherwise, where $\nu_0(\mathrm{He})$ is He I ionization energy in units of eV.

iii) He II:

$$\sigma_\nu(\mathrm{He\ II}) = 7.55 \times 10^{-10} \nu^{-4} \frac{e^{-4(\arctan \epsilon_2)/\epsilon_2}}{1 - e^{-2\pi/\epsilon_2}} \qquad \text{for } \nu \geq \nu_0(\mathrm{He\ II}) \tag{25}$$

and zero otherwise, where $\epsilon_2 = [\nu/\nu_0(\mathrm{He\ II}) - 1]^{1/2}$ and $\nu_0(\mathrm{He\ II})$ is He II ionization energy.

2. Compton heating: When the matter temperature is less than the background radiation temperature (see eq. [17]).
3. Shock heating: Is incorporated into the codes by numerical viscosity, i.e., occurs automatically when shocks form.

2.1.3. *Ionization and Recombination Coefficients* (in $\mathrm{cm^3\ s^{-1}}$)

1. Collisional ionization:

i) H I:

$$\beta_{\rm H}(T) = 5.85 \times 10^{-11} T^{1/2}(1 + T_5^{1/2})^{-1} e^{-157809.1/T}\,, \tag{26a}$$

ii) He I:

$$\beta_{\rm He}(T) = 2.38 \times 10^{-11} T^{1/2}(1 + T_5^{1/2})^{-1} e^{-285335.4/T}\,, \tag{26b}$$

iii) He II:

$$\beta_{\rm He\,II}(T) = 5.68 \times 10^{-12} T^{1/2}(1 + T_5^{1/2})^{-1} e^{-631515/T}\,. \tag{26c}$$

2. Recombination:

i) H II:

$$\alpha_{\rm H\,II}(T) = 8.40 \times 10^{-11} T^{-1/2}\left(\frac{T}{10^3}\right)^{-0.2} \Big/ \left[1 + \left(\frac{T}{10^6}\right)^{0.7}\right] n(e) n(\mathrm{H\,II})\,, \tag{27a}$$

ii) He II:

$$\alpha_{\rm He\,II}(T) = 1.50 \times 10^{-10} T^{-0.6353}\,, \tag{27b}$$

iii) He III:

$$\alpha_{\rm He\,III}(T) = 3.36 \times 10^{-10} T^{-1/2}\left(\frac{T}{10^3}\right)^{-0.2} \Big/ \left[1 + \left(\frac{T}{10^6}\right)^{0.7}\right] n(e) n(\mathrm{He\,II})\,. \tag{27c}$$

3. Dielectronic recombination (He II):

$$\xi_{\rm He\,II}(T) = 1.9 \times 10^{-3} T^{-1.5} e^{-470000/T}(1 + 0.3 e^{-94000/T})\,. \tag{28}$$

4. Photoionization:

i) H I:

$$\frac{\partial \rho_{\rm H\,I}}{\partial t} = -\rho_{\rm H\,I} \int_{\nu_0(\rm H)}^{\infty} 4\pi \sigma_\nu(\mathrm{H}) \frac{i(\nu)}{h\nu}\, d\nu\,, \tag{29a}$$

ii) He I:

$$\frac{\partial \rho_{\rm He\,I}}{\partial t} = -\rho_{\rm He\,I} \int_{\nu_0(\rm He)}^{\infty} 4\pi \sigma_\nu(\mathrm{He}) \frac{i(\nu)}{h\nu}\, d\nu\,, \tag{29b}$$

iii) He II:

$$\frac{\partial \rho_{\rm He\,II}}{\partial t} = -\rho_{\rm He\,II} \int_{\nu_0(\rm He\,II)}^{\infty} 4\pi \sigma_\nu(\mathrm{He\,II}) \frac{i(\nu)}{h\nu}\, d\nu\,. \tag{29c}$$

2.2. *Collisionless Components*

Now we give the set of equations for collisionless pointlike components in comoving coordinates:

$$\frac{d\boldsymbol{x}}{dt} = \frac{1}{a}\boldsymbol{u}\,, \tag{30}$$

$$\frac{d\boldsymbol{u}}{dt} = -\boldsymbol{u}\frac{\dot{a}}{a} - \frac{1}{a}\nabla\phi\,, \tag{31}$$

where $\boldsymbol{x}$ is the comoving coordinates and $\boldsymbol{u}$ is the proper peculiar velocity. The proper peculiar gravitational potential, ϕ, is defined by

$$\nabla^2\phi(\boldsymbol{x}, t) \equiv 4\pi G[\rho_{\rm tot}(\boldsymbol{x}, t) - \rho_0(t)]/a\,, \tag{32}$$

where G is the gravitational constant, $\rho_{\rm tot}(t) \equiv \rho_b(t) + \rho_d(t)$ (ρ_b and ρ_d are the comoving baryonic and dark matter density, respectively), and $\rho_0(t)$ is the comoving background density.

In the FRW universe, the equations governing the homogeneous cosmic background coordinates (cf. Peebles 1980) can be written as

$$\dot{a}^2 = \left[\frac{8\pi G}{3}\rho_0(t) + \frac{\Lambda}{3}\right]a^2 - k\,, \tag{33}$$

$$\ddot{a} = -\left\{\frac{4\pi G}{3}[\rho_0(t) + p_0(t)] - \frac{\Lambda}{3}\right\}a\,, \tag{34}$$

where $\rho_0(t)$ and $p_0(t)$ are the background density and pressure, respectively; k is the space curvature, which has one of three values: -1 for an open universe, 0 for a flat universe, and 1 for a closed universe; and Λ is the cosmological constant. Another equation which we use to check the accuracy of the codes is the cosmic energy equation, which can be written in the following form:

$$a[E(a) + W(a)] = a_0[E(a_0) + W(a_0)] - \int_{a_0}^{a} E\,da\,, \tag{35}$$

where a and a_0 are two scale factors at two different times, and E and W are total energy (peculiar kinetic + thermal) and gravitational energy, respectively. The cosmic energy equation is valid on the assumption that gravitational force is the only energy source term, no other energy loss term is allowed, and the system is large enough so that fluctuations outside have little effect on it.

The formula to calculate the Zel'dovich-Sunyaev effect (Zel'dovich & Sunyaev 1969), according to them, is defined as

$$\begin{aligned} y &\equiv -\int_{t_0}^{t} \frac{kT_e}{m_e c^2}\, n(e)\sigma_0 c\, dt \\ &= \int_0^{\tau} \frac{kT_e}{m_e c^2}\, d\tau\,, \end{aligned} \tag{36}$$

where T_e is the electron temperature, σ_0 is the electron cross section, $n(e)$ is the electron number density, m_e is the electron mass, c is the speed of light, k is Boltzmann's constant, and t is time. A Planckian spectrum which today would give T_0 if undisturbed, is deformed as a result of Compton scattering so that at low frequencies the effective temperature decreases:

$$T_{\rm RJ} = T_0 e^{-2y} \tag{37}$$

(but the frequency dependence remains $F_\nu \sim \nu^2$), and the overall energy of the radiation increases:

$$u = u_0 e^{4y}\,. \tag{38}$$

Other formulae we need are those to calculate the diffuse average radiation spectrum in a whole simulated box due to the free-free and free-bound emissions less absorption. The free-free (or bremsstrahlung) continuum emitted by the free electrons accelerated in Coulomb collisions with positive ions (which are H II, He II, and He III) has an emission coefficient (Rybicki & Lightman 1979) (in units of ergs cm^{-3} s^{-1} Hz^{-1} sr^{-1})

$$j_{\rm ff}(\nu) = \frac{1}{4\pi}\frac{32e^4h}{3m_e^2c^3}\left[\frac{\pi h\nu_0({\rm H})}{3kT}\right]^{1/2} e^{-h\nu/kT} g_{\rm ff}[n({\rm H\ II}) + n({\rm He\ II}) + 4n({\rm He\ III})]n(e)\,, \tag{39}$$

and the recombination (free-bound) emissivities are given below:

i) From H II:

$$j_{\rm fb,H\ II}(\nu) = \frac{h}{4\pi}\frac{1}{kT}\alpha_{\rm H\ II}(T)n({\rm H\ II})n(e)h\nu e^{-h[\nu-\nu_0({\rm H})]/kT}\,, \tag{40a}$$

ii) From He II:

$$j_{\mathrm{fb,He\,II}}(\nu) = \frac{h}{4\pi}\frac{1}{kT}\alpha_{\mathrm{He\,II}}(T)n(\mathrm{He\,II})n(e)h\nu e^{-h[\nu-\nu_0(\mathrm{He\,I})]/kT}, \tag{40b}$$

iii) From He III:

$$j_{\mathrm{fb,He\,III}}(\nu) = \frac{h}{4\pi}\frac{1}{kT}\alpha_{\mathrm{He\,III}}(T)n(\mathrm{He\,III})n(e)h\nu e^{-h[\nu-\nu_0(\mathrm{He\,II})]/kT}, \tag{40c}$$

in units of ergs $\mathrm{cm}^{-3}\,\mathrm{s}^{-1}\,\mathrm{Hz}^{-1}\,\mathrm{sr}^{-1}$, where g_{ff} is a Gaunt factor, which we allow to be a constant equal to 1.5; e is the electron charge; h is Planck's constant; k is Boltzmann's constant; m_e is the electron mass; $\nu_0(\mathrm{H})$, $\nu_0(\mathrm{He\,I})$, $\nu_0(\mathrm{He\,II})$ are H I, He I, He II ionization frequencies, respectively; and T is the electron temperature. Doubly ionized helium, singly ionized hydrogen, and electron density are determined by conservation of $\mathrm{H_{tot}}$, $\mathrm{He_{tot}}$, and charge. We calculate the absorption in an averaged fashion over the whole box due to photoionization of the three species. The absorption coefficient $\kappa(\nu)$ is defined as

$$\kappa(\nu) = n(\mathrm{H\,I})\sigma_\nu(\mathrm{H\,I}) + n(\mathrm{He\,I})\sigma_\nu(\mathrm{He\,I}) + n(\mathrm{He\,II})\sigma_\nu(\mathrm{He\,II}), \tag{41}$$

where $\sigma_\nu(\mathrm{H\,I})$, $\sigma_\nu(\mathrm{He\,I})$, and $\sigma_\nu(\mathrm{He\,II})$ are cross sections, given in equations (23), (24), and (25). Equations (39) and (41), when substituted in equation (7) and averaged over the box, allow us to calculate the evolution of the mean radiation field $i(\nu)$. In evolving the mean radiation field, we explicitly integrate equation (7) using 50 frequency bins, 10 per decade of frequency starting at 1 eV and reaching five decades to 100 keV. Cosmological effects and all relevant bound-free and free-free processes are included. Line radiation processes have not yet been incorporated in the code.

In all, we track six species (e^-, H I, H II, He I, He II, He III), allowing for both radiative and collisional processes which neither ionization nor cooling/heating based on the assumption of thermal or statistical equilibrium. This level of detail, we have found, is necessary if scales less than 100 kpc are to be treated properly. We have found that heating/cooling rates can be misestimated by factors exceeding 10^2 if, for example, collisional ionization equilibrium with a standard $\Lambda_{\mathrm{cooling}}(T)$ is adopted. The price we pay, in addition to the added complexity, is that in certain domains the equations become "stiff" with ideal time steps for thermal processes quite small compared with the appropriate dynamical time scale. We add more discussion of this problem in § 3.

We also calculate the Gunn-Peterson (1965) optical depth and the mean depression of light at that wavelength. The Gunn-Peterson optical depth can be expressed as a function of the density of the neutral hydrogen:

$$\tau_{\mathrm{GP}} = 4.6 \times 10^5 \Omega_{\mathrm{H\,I}} h_0 (1+z)^2 (1+2q_0 z)^{-1/2}, \tag{42}$$

where $\Omega_{\mathrm{H\,I}}$ is the neutral hydrogen density in units of critical density. The mean depression of the continuum just shortward of Lyα is calculated as

$$D_A = 1 - \ln\left(\langle e^{-\tau_{\mathrm{GP}}}\rangle\right), \tag{43}$$

where the angular brackets indicate averaging over the cells of the simulation box, and τ_{H} is the Lyα optical depth of a cell.

3. NUMERICAL TECHNIQUES

The principles on which our numerical algorithm for the baryonic fluid is based were discussed in Jameson (1989) and references therein. In the first step, the ordinary differential equations were transformed into finite-difference equations, which involves space discretization and time difference. Taking equation (4a) as an example to illustrate this procedure, we use cubic box cells throughout our calculations, although any form could be used, and all the variables are defined in the centers of cells. Integrating equation (4a) over the cell labeled i, j, k, we find

$$\frac{d}{dt}\left[\Delta l^3 \rho(i,j,k)\right] + \frac{1}{a}(q+w) = 0, \tag{44}$$

where Δl is the comoving distance of two adjacent cells, q is the net mass flux out of the cell, and w is the equivalent diffusive flux. These fluxes can be written as sums over the cell faces:

$$q = \sum_N f_{i,j,k,N} S_{i,j,k,N}, \tag{45}$$

$$w = \sum_N D_{i,j,k,N} S_{i,j,k,N} , \tag{46}$$

where the sums are over all the faces of cell i, j, k; $S_{i,j,k,N}$ is the directed comoving area of the face separating cell i, j, k from cell N; and the flux $f_{i,j,k,N}$ is evaluated by taking the average of its value in cell i, j, k and cell N.

$$f_{i,j,k,N} = \tfrac{1}{2}(f_{i,j,k} + f_N) , \tag{47}$$

and $D_{i,j,k,N}$ is evaluated as

$$D_{i,j,k,N} = \text{Max}\,(F_{i,j,k}, F_N)(\rho_N - \rho_{i,j,k})/\Delta l , \tag{48}$$

where Max is the function which takes the maximum of the arguments, and the viscous parameter $F_{i,j,k}$ is evaluated as follows. Note that there are three such terms, corresponding to three different directions. Take the x-direction as an example:

$$F_{i,j,k}(x) = \text{VIS}_2(C_{i,j,k} + |u_x|)\left|\frac{p_{i+1,j,k} - 2p_{i,j,k} + p_{i-1,j,k}}{p_{i+1,j,k} + 2p_{i,j,k} + p_{i-1,j,k}}\right| , \tag{49}$$

where $C_{i,j,k}$ is the local speed of sound; u_x is the flow velocity in the x-direction at the cell i, j, k; $p_{i,j,k}$ is the pressure of cell i, j, k; etc. After space and time discretization is done, we are ready to integrate the equations. The integration is by an explicit first-order scheme. Let $\rho^n_{i,j,k}$ be the density of cell i, j, k after n steps. The general form of the density of cell i, j, k at step $n + 1$ is

$$\rho^{n+1}_{i,j,k} = \rho^n_{i,j,k} + (q + w)\frac{\Delta t}{\Delta l^3} . \tag{50}$$

We have also used a fourth-order Runge-Kutta integration scheme and discovered that changes in integrated energy quantities differ by less than 1.0% for the whole run; this indicates that first-order and fourth-order schemes have the same accuracy, since each has an accuracy of 1%–3%. The virtue of a first-order scheme is that it is not necessary to store derivatives of the quantities at intermediate time steps, saving a substantial amount of storage (Binney 1990).

When seeing a hydrodynamic mesh code, the first question asked by a programmer is: How does the code incorporate the numerical viscosity into it? Let us explore this subject now in somewhat greater detail. The effect of dissipation on shocks has been studied by various investigators. When heat conduction is allowed for, the temperature varies smoothly through the shock layer for shocks of strength less than a critical value, and the pressure and density vary smoothly also, whereas, for stronger shocks, the transition of pressure and density from their initial to final values is partly by a smooth variation and partly by a discontinuous jump. When viscosity is allowed for, however, all quantities vary smoothly through the shock region for a shock of any strength. In either case, the thickness of the transition zone is proportional to the coefficient of the dissipative mechanism, so that in the limit of no heat conduction and no viscosity, the variations should approach the discontinuous ones of the Hugoniot theory.

The idea of von Neumann and Richtmyer (von Neumann & Richtmyer 1950; Richtmyer 1957) was to introduce a purely artificial dissipative mechanism of such form and strength that a shock transition would be a smooth one extending over a small number (say three or four) of cells, and then to construct finite-difference equations with the diffusion included but without any necessity of shock fitting. In a calculation with such equations, the shocks show up automatically as near-discontinuities, across which quantities have very nearly the correct jump, and which travel at very nearly the correct speed through the fluid.

The hydrodynamic equations without any dissipation terms will allow undamped oscillations, i.e., sound waves. In order to eliminate spurious oscillations, which will be triggered by discontinuities in the solution, enough diffusion is needed to control the tendency to produce spurious oscillations in the undamped original equations. A standard form for numerical diffusion in the x-direction is the following:

$$q = \tfrac{1}{2}\text{VIS}_1\rho[u_x(I + 1) - u_x(I - 1)]^2 \qquad \text{for} \qquad [u_x(I + 1) - u_x(I - 1)] < 0 , \tag{51}$$

as the sensor for x-direction shock waves; otherwise q is zero. Then q is added to the pressure term p. The total dissipation is the summation of the three similar terms of the three directions. VIS_1 is a constant about unity.

In our codes, a diffusion term like equation (51) is not used. Instead we use an adaptive scheme for adding diffusion which has proved effective in practice. The idea of the adaptive scheme is to add third-order dissipative terms (A_3) which are defined as

$$A_3(\text{Var}) \equiv \text{VIS}_4(C + |u_k|)(\Delta l)^3 \frac{\partial^3 \text{Var}}{\partial x_k^3} , \tag{52}$$

where VIS_4 is a constant and Var is relevant variables, which can be density, momentum, or energy. Throughout the domain, these third-order terms provide a base level of diffusion which is sufficient to prevent nonlinear instability but which is not sufficient to totally prevent oscillations in the neighborhood of shock waves. In order to capture shock waves, additional first-order diffusive terms (A_1, i.e., the terms defined in eqs. [11a]–[11c], i.e., $A_1(\rho) = D_{\rho k}$, etc.) are added locally by a sensor designed to detect shocks.

An effective sensor for the presence of a shock wave can be constructed by taking the second derivative of the pressure. Define the dimensionless quantity

$$\Sigma_{i,j,k} \equiv \left| \frac{p_{i+1,j,k} - 2p_{i,j,k} + p_{i-1,j,k}}{p_{i+1,j,k} + 2p_{i,j,k} + p_{i-1,j,k}} \right| , \tag{53}$$

as the sensor for x-direction shock waves, and similar ones for the y- and z-directions. If there is no shock, $\Sigma_{i,j,k}$ is a second-order term. When this second-order term is multiplied by a first-order coefficient, it becomes a third-order term, which is the same order as the base level dissipative term. But in the regions where there are shocks, $\Sigma_{i,j,k}$ is of order unity, times a first-order coefficient, so this scheme behaves locally like a first-order scheme. However, in practice the second viscous term A_1 itself is usually sufficient to prevent nonlinear instability. The reason is that it behaves like a third-order dissipative term in the regions where there is no shock. So we choose to use only the second viscous term A_1, which leads to the final forms as in equations (10) and (11a)–(11c). For a more detailed description of the viscous terms see Jameson (1989) and references therein.

The time step is determined by the Courant condition

$$\Delta t = \text{Min}\left(\frac{\text{CFL} \times a \times \Delta l}{|\boldsymbol{u}| + C} \right), \tag{54}$$

where Min is the function which takes the minimum value among all the cells. CFL is the Courant number, which we allow to have a value less than unity, Δl is the comoving cell size, a is the expansion scale parameter, $\boldsymbol{u}$ is proper peculiar velocity, and C is the local sound speed. In practice, we use the minimum of the following three times: (Δt_1, Δt_2, Δt_3); Δt_1 is the smallest time step determined by equation (54) among all cells with CFL = 1.0; Δt_2 is the twentieth smallest time step determined by equation (54) among all cells with CFL = 0.6; and Δt_3 is the preset time step, so that $\Delta a/a < 0.01$. The reason for this scheme is obvious. It is impractical to slow down the whole calculation because of the behavior of a very small number of cells.

Equations (4b)–(4d) and (6) are likely to be stiff (cf. Press et al. 1986, p. 572; Acton 1970, p. 148). They are liable to severe oscillations which may even lead to the stopping of the program if an explicit (or *forward*) Euler scheme for integration is used. Take a very simple equation as an example:

$$\dot{y} = -cy , \tag{55}$$

$$y_{n+1} = y_n + \Delta t \dot{y}_n = (1 - c\Delta t) y_n . \tag{56}$$

The method is called "explicit" because the new value y_{n+1} is given explicitly in terms of the old value y_n. Clearly the method is unstable if time step $\Delta t > 2/c$, for then $y_n \to \infty$ as $n \to \infty$. If c oscillates in sign as y is bigger or smaller than some equilibrium value, then equations (55) and (56) are stable if sufficiently small time steps are taken. But these steps may be inconveniently small (for example, if these are thermal equations and the heating/cooling time scale is small compared with the dynamical time scale), and the use of too large a time step would lead to wild, unphysical oscillations. The simplest cure is to resort to implicit differencing, where the right-hand side is evaluated using the *new* y. In this case, we have the *backward* Euler scheme:

$$y_{n+1} = y_n + \Delta t \dot{y}_{n+1} \tag{57}$$

or

$$y_{n+1} = \frac{y_n}{1 + c\Delta t} , \tag{58}$$

which is an approach recommended in Numerical Recipes. We have experimented with other, still more stable methods of solving this kind of equations, which we have implemented as follows:

$$y_{n+1} = y_n / [1 + \ln (1 + |c| \Delta t)]^{\text{sign}(c)} \tag{59}$$

and

$$y_{n+1} = y_n \left[1 - \frac{1}{\pi} \arctan (\pi c \Delta t) \right] , \tag{60}$$

and c can be either positive or negative. Equations (58), (59), and (60) all reduce to equation (56) in the limit of small time step, as

they must, but produce smaller changes than the linear model (56) when $|c\Delta t| \gg 1$. We use equation (60) to incorporate this technique in the explicit integration scheme when needed to stabilize the scheme without sacrificing much accuracy of the code. The reason why we need to employ this technique is that in our calculation five quite different time scales are involved. The first is the time scale determined by the Courant condition (cf. eq. [54]), which is basically the information exchange time scale between adjacent cells. To avoid spurious effects due to unnecessary information exchange between nonadjacent cells, the time step must be less than this; usually it is some fraction of it. The second time scale is the cooling time scale due to various processes which are proportional to $(1 + z)^{-6}$, except for Compton cooling, which is proportional to $(1 + z)^{-4}$. So at early epochs this time could be quite small. The third time scale is the ionization time scale of hydrogen and helium and is comparable to the second time scale. The fourth time scale is the Hubble time, which is proportional to $(1 + z)^{-3/2}$ and is roughly the age of the universe. The fifth time scale is the gravitational free-fall time of a dense system, and could be significantly less than the Hubble time if the subsystem is quite overdense. The time step used in our calculations is determined by the Courant condition (cf. eq. [54]). Therefore, we have to implement the techniques of solving stiff equations if some other time scales are much less than that, which is usually true for the cooling time scale in early epochs. Of course, we could have used the minimum of these five time scales, but this would require vast amounts of computing time if one of these time scales were much less than that determined by the Courant condition; this turns out to be impractical. The reason why this approximation will not sacrifice much accuracy is that whenever this happens, the region involved will cool down to an equilibrium temperature of 10^4 K or less (about the peak of the cooling curve due to hydrogen collisional excitation cooling), and it will maintain itself at near the equilibrium state of temperature and ionization before there is any significant change in its density and velocity. This is basically the virtue of the techniques of solving stiff equations. In other words, approaching the true value smoothly rather than violently with oscillations is a much better method and is not much worse than using a much smaller time step. The same reason applies to the case when ionization time is much less than that determined by the Courant conditions. Nevertheless, ionization or recombination times may be smaller or bigger than the cooling time. In the latter case, ionization equilibrium breaks down. We use the same method for all these stiff situations; hence, oscillations will be minimized, and the overall evolution should not be much affected.

We use the particle-mesh method to solve the motion of collisionless dark matter particles. The densities on the grids due to dark matter particles are assigned using CIC (cloud-in-cell) techniques (cf. Efstathiou et al. 1985). The density due to a particle is assigned to its nearest eight cells by constructing a cubic cloud centered on the particle. Then the density contribution from this particle to a cell is the fractional volume of this constructed cloud in the cell. The gravitational forces on dark matter particles are calculated in the same way, but procedurally opposite. The fractional contribution from a grid to the force of a particle is the fractional volume of this constructed cloud in the cell centered at that grid. The positions and velocities of dark matter particles are advanced sharing the same first-order integration scheme as that for the baryon fluid component.

Periodic boundary conditions are used throughout all the simulations. The Poisson equation (eq. [32]) is solved using the standard fast Fourier transform (FFT) method in the following manner. First, we forward Fourier-transform (FT) the density field $\rho(\boldsymbol{x})$ to get $\hat{\rho}(\boldsymbol{k})$; second, we compute $\hat{\phi}(\boldsymbol{k})$ from $\rho(\boldsymbol{k})$; third, we backward FT $\hat{\phi}(\boldsymbol{k})$ to get $\phi(\boldsymbol{x})$; fourth, we difference $\phi(\boldsymbol{x})$ to get the force field at centers of cells and at centers of faces separating cells. For the fluid part, the force felt by a cell is just the force at that point calculated above. For a dark matter particle, the force felt by it is calculated in the following way. (We take a two-dimensional case as a simple example to illustrate this procedure.) We know the x-direction forces at points a, b, c, d are $f_x(a), f_x(b), f_x(c), f_x(d)$, and the y-direction forces at points 1, 2, 3, 4 are $f_y(1), f_y(2), f_y(3), f_y(4)$; then the x- and y-direction forces felt by the particle P are calculated as

$$f_x(P) = \frac{S_1 f_x(a) + S_2 f_x(b) + S_3 f_x(c) + S_4 f_x(d)}{S_1 + S_2 + S_3 + S_4}, \tag{61}$$

$$f_y(P) = \frac{s_1 f_y(1) + s_2 f_y(2) + s_3 f_y(3) + s_4 f_y(4)}{s_1 + s_2 + s_3 + s_4}, \tag{62}$$

where $S_1, S_2, S_3, S_4, s_1, s_2, s_3$, and s_4 are the areas shown in Figure 5. For the three-dimensional case, we use the same technique, but the force in each direction felt by a particle is volume-weighted over eight nearest relevant points. Resolution is higher in our dark matter PM code for the following reason. Two particles within a cell cannot feel gravitational interaction from each other because of the nature of the PM code if the density contribution of a particle is entirely assigned to the cell where the particle is located, i.e., smoothing length is effectively one cell size. However, the effective smoothing length of this PM code is somewhat less than a cell size owing to the fractional density assignment scheme, i.e., the CIC technique. In other words, two particles within a cell can still feel some fractional interaction between them although it is less than it should be. But the fluid mesh code has an effective smoothing length of one cell size. For this reason we smooth the density of dark matter slightly to compensate this effect when we compute dark matter density for final output; we will go back to this problem in § 5.

Now let us address how the radiation field (cf. eq. [7]) is solved. We solve equation (7) by a first-order time-explicit integration scheme. A total of 50 frequency bins are used in the range of 1 eV to 100 keV. At each time step, the mean emissivity $j(\nu)$, as a function of frequency, is calculated by adding the contributions from all the cells due to bremsstrahlung and recombination processes (cf. eqs. [39] and [40a]–[40c]) to each frequency bin, and the mean absorption coefficient $\kappa(\nu)$ is computed using equation (41) by averaging the individual absorption coefficient of each cell in the whole box. The evolution of the mean intensity at each frequency is thus calculated by averaging all quantities over the box, as would be appropriate in the optically thin limit.

4. INITIAL CONDITIONS

The initial conditions for Gaussian processes, i.e., processes in which the phases of the waves are random and uncorrelated, are determined in the following manner: given a power spectrum $P(k)$, the amplitude of the power spectrum is usually chosen to fit observations of galaxy clustering and peculiar velocities. We adopt the method used by Weinberg & Gunn (1990). The rms linear density fluctuation in an $8h^{-1}$ Mpc sphere σ_8 is

$$\sigma_8^2 = \int_0^\infty 4\pi k^2\, dk\, P(k)\, \hat{W}_{\rm TH}^2(k)\,, \tag{63}$$

where $\hat{W}_{\rm TH}$ is the Fourier transform of a spherical window of radius $R = 8h^{-1}$ Mpc,

$$\begin{aligned}\hat{W}_{\rm TH}(k) &= \left(\frac{4\pi R^3}{3}\right)^3 \int_0^\infty d^3r\,\Theta\left(\frac{1-r}{R}\right) \exp\left(-2\pi i \boldsymbol{k}\cdot\boldsymbol{r}\right) \\ &= \frac{3[\sin(2\pi kR) - 2\pi kR\cos(2\pi kR)]}{(2\pi kR)^3}\,,\end{aligned} \tag{64}$$

and Θ is the step function as

$$\Theta(x) = \begin{cases} 1 & \text{for} \quad x \geq 0 \\ 0 & \text{for} \quad x < 0\,. \end{cases} \tag{65}$$

A standard "unbiased" normalization condition is

$$\sigma_8 = 1\,, \tag{66}$$

because the two-point correlation function derived by Davis & Peebles (1983) from the CfA redshift survey implies rms galaxy count fluctuations in the $8h^{-1}$ Mpc sphere equal to unity. Even if the normalization is determined in some other way, e.g., by fitting the cluster velocity dispersion, the slope of the galaxy-galaxy two-point correlation function, or large-scale peculiar velocities, σ_8 is still a useful parameter for expressing the amplitude of the normalized power spectrum.

It was argued by some that galaxies prefer to form in high peaks of the initial density field, i.e., galaxies are biased to the underlying mass distribution (cf. Bardeen et al. 1986, hereafter BBKS). If so, then galaxies now cluster more strongly than the mass. In that case we would have overestimated the amplitude of the power spectrum by a bias factor b, so instead the correct normalization should be

$$\sigma_8 = \frac{1}{b}\,, \tag{67a}$$

since by hypothesis

$$\left(\frac{\delta N}{N}\right)_{\rm galaxy} \equiv b\left(\frac{\delta M}{M}\right)_{\rm total}\,. \tag{67b}$$

We adopt this prescription and define the amplitude of the power spectrum to be such that equation (67a) is satisfied or $(\delta M/M)_{\rm rms} = 1/b$ in $8h^{-1}$ Mpc spheres at $z = 0$. Other physical mechanisms for biasing have also been proposed (cf. the review by Dekel & Rees 1987, White et al. 1987a,b, and Kaiser 1988). Fortunately, the qualitative effects of biasing are not particularly sensitive to the details of various schemes. After studies of the present three-dimensional topology of the large-scale structures—which has the following characteristics: large voids of size $\sim 50h^{-1}$ Mpc separated by ridges, filaments, and sheets, where galaxies, clusters of galaxies, and superclusters exist—Weinberg (1990) pointed out that biasing may be a necessary ingredient if any gravitational instability model is to reproduce the frothy texture of the observed galaxy distribution. Note here that "bias" is assumed only in our initial normalization in order to fix the amplitude of the power spectrum. All output quantities are given unfiltered, i.e., exactly as computed. Thus, in the end we can, in principle, check whether there is really a bias of the type assumed in equation (67b).

After we have obtained the normalized theoretical power spectrum $P(k)$, we multiply it by a filter $F(k)$,

$$P_F(k) = P(k)F(k)\,, \tag{68}$$

where $F(k)$ has the form

$$F(k) = \cos^{1/4}(\pi k/2k_{\rm Nq})\,, \tag{69}$$

where k_{Nq} is the Nyquist frequency; for a box with N cells per side, $k_{Nq} = N/2$. In our units $k = 1$ corresponds to a wavelength of the box size. This filter has the following properties: it makes the power go smoothly to zero at the Nyquist frequency but has small effect at other frequencies; less dynamic range is lost with this filter than with the standard "Hanning" cosmic filter (cf. Press et al. 1986, p. 425, for the necessity of using filters to prevent power leakage of frequency bins into nearby bins). With this filtered power spectrum $P_F(k)$, we generate a Gaussian random density field using the scheme described in Efstathiou et al. (1985). Here we briefly describe this technique. The amplitude of each mode of the spectrum in Fourier space is random but has a normal distribution with zero mean and variance determined by the prescribed power spectrum $P_F(k)$. The phase is also random but is uniformly distributed in the range $0-2\pi$. Of course we have discretized the continuous power spectrum into a limited number of modes due to the grid. But we believe that all the main features should remain, and when the grid spacing gets smaller and smaller, we expect that it will asymptotically approach the real continuous case. The code does the following operation to initialize the conditions: each mode is assigned as

$$\hat{\rho}(\boldsymbol{k}) = \left[\frac{P_F(k)}{2}\right]^{1/2} (R_1 + iR_2) , \tag{70}$$

where R_1 and R_2 are random numbers with normal distribution and unit variance, and $i = \sqrt{-1}$. Since the Fourier transform of a real array of density should be a half-complex array, it is necessary to adjust the initial array $\hat{\rho}(\boldsymbol{k})$ to satisfy the complex conjugate symmetry conditions. Then we make an inverse Fourier transform to get the density field $\rho_{z=0}(\boldsymbol{r})$ at $z = 0$. Next we linearly extrapolate $\rho_{z=0}(\boldsymbol{r})$ back to the starting epoch $z = z_{\rm init}$ to get the initial density fluctuations, i.e., assuming that the linear perturbation theory is correct on the normalizing scale that we use, which is $8h^{-1}$ Mpc,

$$\rho_{z_{\rm init}}(\boldsymbol{r}) = \frac{g(z_{\rm init})}{g(0)} \rho_{z=0}(\boldsymbol{r}) , \tag{71}$$

where $g(z)$ is the amplitude of density fluctuation at epoch z according to linear theory. The initial peculiar velocity field is obtained by Zel'dovich approximation (cf. Zel'dovich 1970), which Zel'dovich formulates in the following way: the trajectory of a particle under the gravitational force of the density fluctuation is

$$\boldsymbol{r}(\boldsymbol{x}, t) = a(t)[\boldsymbol{x} + g(t)\boldsymbol{p}(\boldsymbol{x})] , \tag{72}$$

and the proper peculiar velocity is

$$\dot{\boldsymbol{r}}(\boldsymbol{x}, t) - \dot{a}\boldsymbol{x} = a(t)\dot{g}(t)\boldsymbol{p}(\boldsymbol{x}) . \tag{73}$$

Equations (72) and (73) are Zel'dovich approximations for particle positions and proper velocities, where $\boldsymbol{x}$ is the comoving coordinates, $a(t)$ is the expansion parameter, $g(t)$ is the fluctuation amplitude parameter, and $\boldsymbol{p}(\boldsymbol{x})$ is the initial displacement of particle positions for the otherwise smooth universe because of the linear gravitational acceleration. It is the gradient of a potential function which is proportional to the peculiar gravitational potential as

$$\boldsymbol{p}(\boldsymbol{x}) = \nabla_{\boldsymbol{x}}\phi , \tag{74}$$

where

$$\nabla_{\boldsymbol{x}}^2\phi = 4\pi G a^2 \delta ; \tag{75}$$

δ is a small density perturbation ($\equiv \rho/\langle\rho\rangle - 1$).

5. TESTS OF THE CODE

We have made the following tests of the code.

5.1. *The One-dimensional Shock Tube Test* (cf. Sod 1978)

The hydrodynamic code is very good at handling high Mach number shocks, showing an effective resolution of approximately 4 cells (for pressure increase by a factor of 10). We show here a one-dimensional shock tube test with Mach number about 1.6. The test is as follows: A diaphragm at the middle separates two regions (regions 1 and 5) which have different densities and pressures. The two regions are in a constant state. The initial conditions are $p_1 > p_5$, $\rho_1 > \rho_5$, and $u_1 = u_5 = 0$; i.e., both fluids are initially at rest. At time $t = 0$, the diaphragm is broken. Consider the case before any wave has reached the left or right boundary. Points x_1 and x_2 represent the location of the head and tail of the rarefaction wave (moving to the left). Although the solution is continuous in this region (region 2), some of the derivatives of the fluid quantities may not be continuous. The point x_3 is the position that an element of fluid initially at the middle has reached by time t. Point x_3 is called a contact discontinuity. It is seen that across a contact

discontinuity the pressure and the normal component of the velocity are continuous. However, the density and the specific energy are not continuous across a contact discontinuity. Point x_4 is the location of the shock wave (moving to the right). Across a shock all of the quantities (ρ, v, e, p) will in general be discontinuous. For this test we choose the following initial conditions and parameters: $\rho_1 = 1, p_1 = 1, u_1 = 0, \rho_5 = 0.125, p = 0.1, u_5 = 0$; the ratio of specific heats γ is chosen to be 1.4, and the grid size $\Delta l = 0.0078$ is used. Figures 1*a*–1*d* show the density, pressure, velocity, and temperature profiles at time $t > 0$. The circles are the numerical results, and solid lines are the analytic results. They show that the shock front and the rarefaction wave travel at the correct speed, and the code can capture a fairly clean strong shock with shock width about 3–4 cells; the discontinuity of density at point x_3 is also represented cleanly.

Let us make a comparison of our shock tube test with the results of a shock tube test using SPH (cf. Fig. 2 of Hernquist & Katz 1989). In their slightly lower Mach number shock tube test, about 10 particles are needed to represent a shock front as well as a contact discontinuity, to be compared with about 4 cells in our code. Both codes produce about the same amount of postshock oscillations in the velocity profile (3%). The oscillations of other quantities in the postshock regions are much smaller in both cases.

5.2. *One-dimensional Caustic ("Pancake") Evolution*

Initially the one-dimensional density distribution is uniform, i.e., there is no initial density perturbation. The velocity distribution has the following form:

$$v_x(t = 0) = \frac{1}{2\pi} \sin(2\pi x), \tag{76}$$

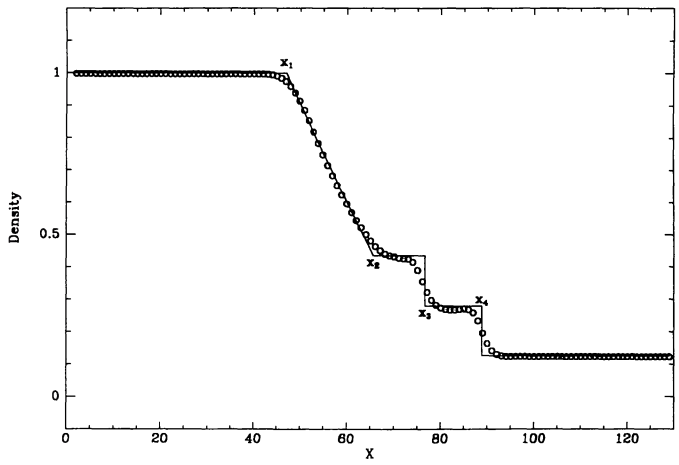

FIG. 1*a*

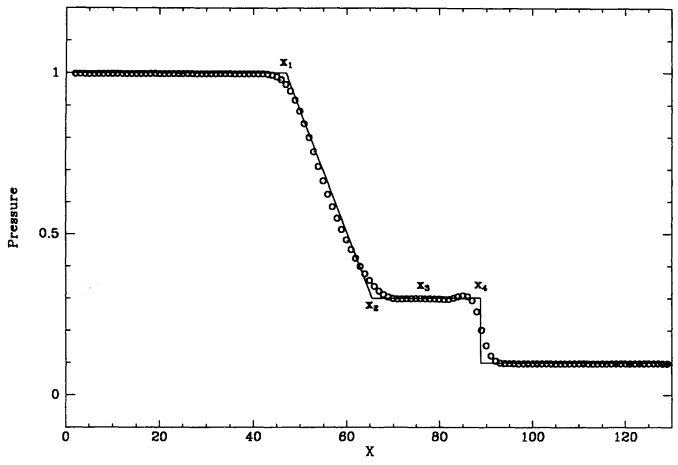

FIG. 1*b*

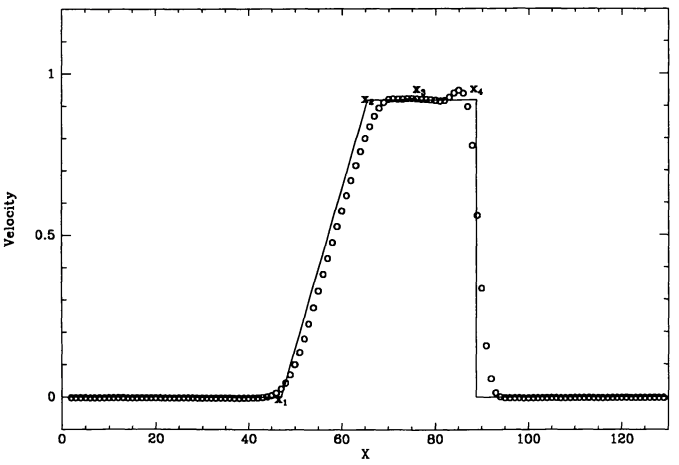

FIG. 1*c*

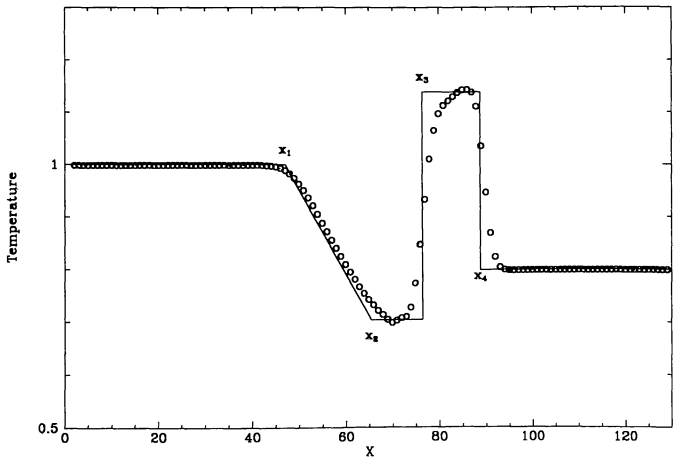

FIG. 1*d*

FIG. 1.—(*a*) Density, (*b*) pressure, (*c*) velocity, and (*d*) temperature profiles at a time $t > 0$. The circles are the numerical results, and solid lines are the analytic results. They show that the shock front and the rarefaction wave travel at the correct speed, the code can capture a fairly clean strong shock with shock width about 3–4 cells; the discontinuity of density at point x_3 is also represented cleanly.

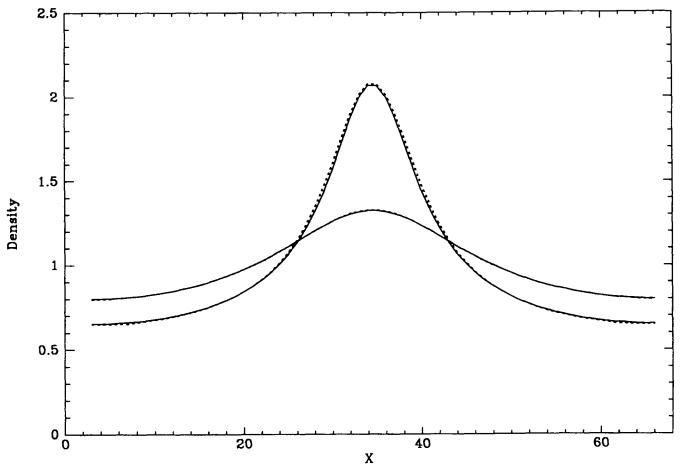

FIG. 2a

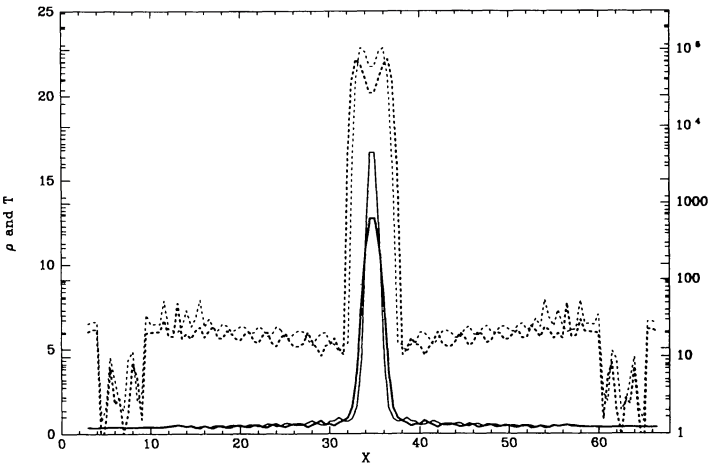

FIG. 2b

FIG. 2.—(*a*) Comparison of numerical results and analytic results of the one-dimensional sine wave caustic collapse evolution before shocks appear. The two solid lines are the computed results at two times, and the dotted lines are the corresponding analytic calculations. (*b*) Comparison of numerical results and analytic results of the one-dimensional sine wave caustic collapse evolution after shocks appear. The two solid lines are the computed results at two times, and the dotted lines are the corresponding analytic calculations.

where x runs from 0 to 1. Note that gravitational force is not included in this calculation, contrary to the calculations in Bond et al. (1984) and Shapiro & Struck-Marcell (1985): Figure 2*a* shows the density distribution of the one-dimensional caustic evolution at two later times before shocks occur. The solid lines are the computed results, and the dotted line shows the analytic results. The figure shows that the computed results agree very well with the analytic calculations. Figure 2*b* shows the density and temperature distributions at postshock epochs. As one may note, the density in the central plane becomes higher and higher as evolution goes on, while the temperature in this plane has a shape of a well, i.e., has a central minimum. The reason is that temperatures of shock-heated regions are independent of their initial temperatures, but are only dependent on the incident shock velocities, provided that initial temperatures are much lower than the corresponding velocities. Matter coming in later has large velocities in this realization; thus, later shocked regions have higher temperatures and lower densities, since pressure within the shocked region is fairly constant (cf. Bond et al. 1984).

5.3. *Three-dimensional Compensated Hole Evolution*

The computed evolution of the three-dimensional shell is in agreement with Bertschinger's calculation (cf. Bertschinger 1985). The dark matter shell is about two times thicker than the baryon shell if we define the width as the separation of the two half-maximum points, and is weakly unstable to nonaxisymmetric modes (cf. White & Ostriker 1990). Figure 3*a* shows the shell profiles of both the baryon shell and the dark matter shell at initial epoch $z = 200$, and at final epoch $z = 0$. The light and dark solid lines are baryonic shell profiles at $z = 200$ and $z = 0$, and the light and dark dotted lines are dark matter shell profiles at $z = 200$ and $z = 0$. The width of the dark matter shell is about twice that of the baryonic shell at the final time, as it should be. The short-dashed line is the analytic solution of a baryonic shell in the $\Omega = 1$, $\Omega_b \ll 1$ case (cf. Table 3 of Bertschinger 1985). Our computed shell is wider by a factor of 3 than the analytic shell solution. This is in part due to the numerical diffusion in the hydrodynamic code and in part due to the limited resolution, noting that our shell occupies only about 4 cells. A 4 times higher resolution run should reach agreement with the analytic solution very well. The two vertical long-dashed lines indicate the position of the dark matter collisionless shell; the internal fine structures (cf. Fig. 3 of Bertschinger 1985), which appear in the analytic solution, do not show up in the simulation because of limited resolution, but the thickness of the dark matter shell agrees well with the analytic solution. The azimuthal oscillations of the density of the dark matter component are initially simply due to the discrete density assignment scheme we employed, which is the CIC scheme. These at later times drive a true (if weak) instability (Hwang, Vishniac, & Shapiro 1989; White & Ostriker 1990; Blaes, Goldreich, & Villumsen 1990). In the regions of dilute density, only a few particles are present, leading to inaccuracy of the CIC scheme. Figure 3*b* shows the accuracy of the calculation over the whole run. The vertical coordinate is the ratio of computed total energy (gravitational energy plus kinetic and internal energy) to the analytic value, which is calculated by the cosmic energy equation. As it shows, accuracy of 3% is achieved. Figure 3*c* shows the six parallel slices of the baryonic shell, Figure 3*d* shows the six parallel slices of the dark matter shell; Figure 3*e* shows one amplified slice of the baryonic shell; and Figure 3*f* shows one amplified slice of the dark matter shell. Note that the baryonic component clumps less than the dark matter component. This is presumably due to the isotropic pressure in the baryonic fluid. The dark matter has a small velocity dispersion in the two directions parallel to the shell and is more unstable to azimuthal motions. Thus we have the apparently paradoxical result that the dark matter has a higher rms density (i.e., is more clumped) even though the dark matter shell is thicker than the gas shell.

5.4. *Comparison of Our PM Codes with Other Particle Codes* (e.g., Park 1990)

The results are almost identical in the void regions, as expected. The difference in dense regions is due to the slightly different techniques utilized in various codes for computing the gravitational force. This test is qualitative. It shows that we have made no gross errors in coding the gravitational potential and the cosmology.

5.5. *Real Simulations with No Cooling Processes Included*

The cosmic energy equation is used to follow the evolution of energy in the simulations. A 64^3 box and the BBKS CDM spectrum are used, with $\Omega = 1.0$, $\Omega_b = 0.1$, normalized so that $(\Delta M/M)_{\rm rms} = 1$ on a top hat $8h^{-1}$ Mpc sphere at $z = 0$. We found that the accuracy is within 1%. When 100% baryon or 100% dark matter is used, a similar accuracy is achieved.

5.6. *Experiments Testing the Effect of the Code on Density due to Numerical Diffusion*

We made two standard runs, 64^3 box simulation and 128^3 box simulation. On each run we used the standard (cf. Weinberg et al. 1991) initial realization of a CDM power spectrum for a 64^3 box. The box's physical size is $64h^{-1}$ Mpc; h is taken to be 0.5; $\Omega = 1$; $\Omega_b = 0.1$; Compton and bremsstrahlung cooling (or heating) terms are included; the runs started at $z = 25$. In other words, the two runs have exactly the same initial input power; the only difference is the resolution. In Table 1 we have binned the 128^3 cells to 64^3 cells to be comparable. The density fluctuations are listed at three epochs. The dark matter rms density fluctuations at the cell scale are with extra smoothing to compensate for the CIC scheme. We used a Gaussian smoothing of length 0.2 cell size in the 128^3 run after 128^3 cells have been binned down to 64^3 cells, and a Gaussian smoothing of length 0.4 cell size in the 64^3 run. These smoothing lengths are adequate to compensate for the effect of the approximate procedure in the CIC scheme of density assignment to the grids according to our tests. The reason follows: take a one-dimensional simple case as an example, assuming only three cells and one particle, and periodic boundary conditions (see Fig. 6). When the particle goes from point A to point B, the rms density fluctuation on the cell scale changes from 1.225 to 1.732. But obviously this kind of change is simply due to the scheme. There is no real change in the rms density fluctuation on the cell scale, which is easily seen if you construct another set of cells shifted by $\frac{1}{2}$ cell size. The same argument can be applied to three-dimensional cases. The Gaussian smoothing with the smoothing length we choose above will make this kind of artificial change almost disappear. In Table 1, σ(fluid) and σ(dark) are the density fluctuations of the baryonic matter and dark matter respectively, on the scale of $1h^{-1}$ Mpc. If we compare the values

$$\frac{\sigma_M(\text{fluid}):128}{\sigma_M(\text{fluid}):64} = 1.405 \quad \text{and} \quad \frac{\sigma_M(\text{dark}):128}{\sigma_M(\text{dark}):64} = 1.312$$

at $z = 0$, we conclude that the smoothing due to artificial viscosity of the hydrodynamic code on the 1 cell scale must be less than 15% [$=2(1.405/1.312 - 1)$; if on the 1 cell scale the smoothing factor is f, then on scales of 2 cell sizes, the smoothing should be $f^{1/2}$]. That is, in the 128^3 run the smallest scale is twice as small as in the 64^3 run, so Compton and bremsstrahlung cooling should be more important in the former run, since the smaller scale goes nonlinear first. Compton cooling is proportional to $(1 + z)^4$ and bremsstrahlung cooling to $(1 + z)^6$; therefore, cooling processes should have induced more collapsing in the former run, which would contribute to the density fluctuations on the scale of 2 cell sizes in the former run (which is the same scale of cell size in the later run). Therefore, for this specific test, 15% is the maximum effect on the average quantities due to artificial viscosities on the cell scale. Furthermore, the artificial viscosity should have a decreasing effect on the large scales. In the first test we saw that a very strong shock having a width of 3–4 cells tells us that smoothing due to the numerical diffusion should be negligible on scales larger than 4 cells. The rms density fluctuation is smoothed out by the numerical diffusion, and the effect can be parameterized as follows:

$$\frac{\sigma_b}{\sigma_d}(N, x) = \left(\frac{\sigma_b}{\sigma_d}\right)_{\rm true}(N, x) - \frac{A}{N}\, e^{-x_s/x}, \tag{77}$$

where N is the number of cells in each direction of a simulated box, x_s is the effective Gaussian length in units of a cell size, x is the scale on which the density fluctuation is calculated, and $(\sigma_b/\sigma_d)_{\rm true}(N, x)$ is the true value if there is no diffusion included in the code. The reason we use the ratio of the two densities is to eliminate the effect of the nonlinear density evolution, since we are now purely concerned with the numerical diffusion effect. Table 2 lists the rms density fluctuation on the scale of $4h^{-1}$ Mpc of three CDM simulations with box size $L = 64h^{-1}$ Mpc and $h = 0.5$, $b = 1.0$. They all have the same initial power spectrum except that in the 32^3 run powers of scales less than $4h^{-1}$ Mpc are eliminated. We binned 8 cells in each direction of the final output of the 128^3 run into one cell, binned 4 cells into one in the 64^3 run, and binned 2 cells into one in the 32^3 run.

Using equation (77), we found that $A = 2.26$, $x_s = 0.6$ and $(\sigma_b/\sigma_d)_{\rm true} = 0.850$ on the $4h^{-1}$ Mpc scale. This gives the result that the effects of numerical smoothing on 2, 4, and 8 cell scales are 6.5%, 3.7%, and 1.9%, respectively. We expect that on the 1 cell scale it is about 15%–20%, which is consistent with the estimate we made above.

One can see that

$$\frac{\sigma_M(\text{dark}):128}{\sigma_M(\text{dark}):64} = 1.312,$$

which is bigger than unity. The reason is that, although the initial density field is Gaussian and random, when the evolution proceeds, the coupling between different modes gets stronger, and the nonlinear property of the equations induces a constant transferral of power from larger scales to smaller scales. Therefore, the smaller the cell size, the more power of larger scales can be transferred to the smaller scale. In other words, contributions of smaller scales to the fluctuations of the density field of larger scales are not negligible because of the nonlinear property of evolution of scales less than a certain size (cf. Carlitz, Frautschi, & Nahm 1973; Press & Schechter 1974; Muchet et al. 1988).

Figures 4*a* and 4*b* show the density contours of the 64^3 and 128^3 runs at $z = 0$. They show that the main structural features remain the same, although there are more features which appear in the latter because of the higher resolution. Figures 4*c* and 4*d* show the

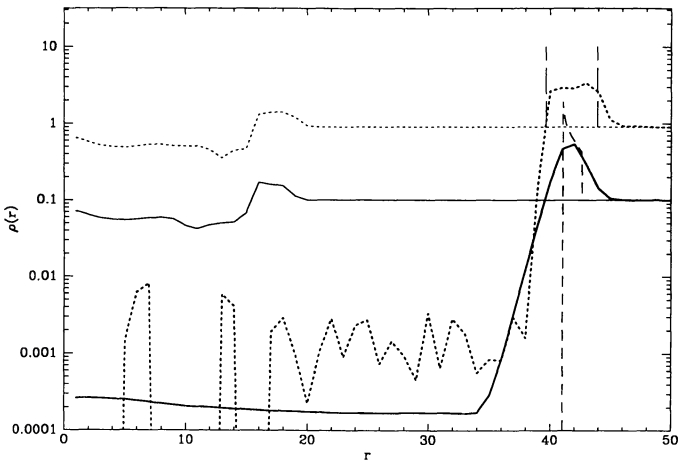

FIG. 3*a*

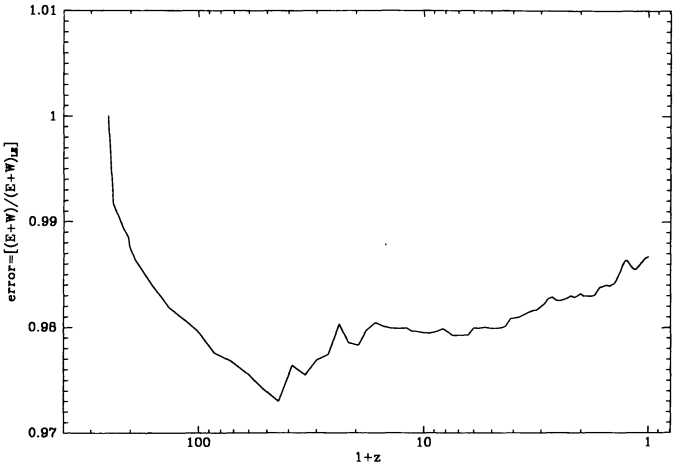

FIG. 3*b*

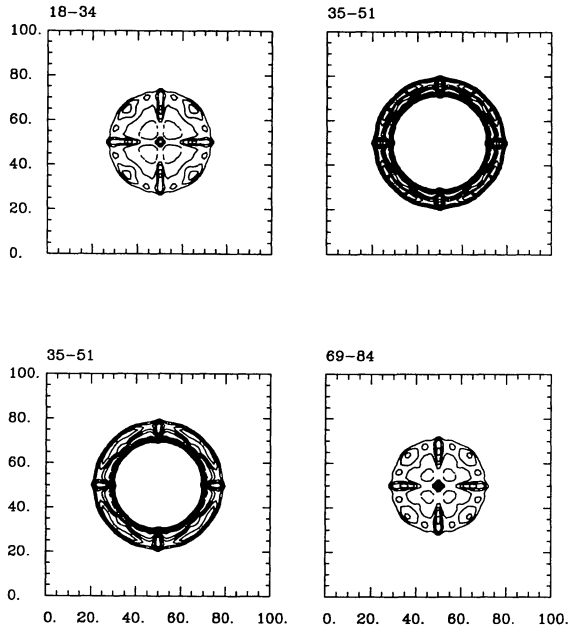

FIG. 3*c*

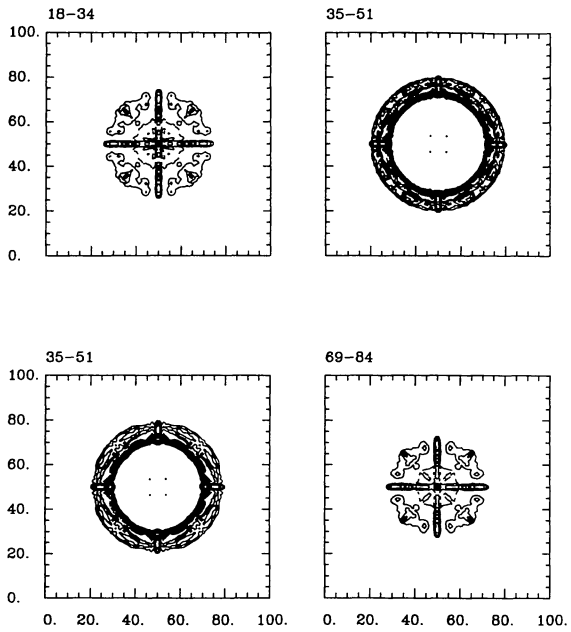

FIG. 3*d*

FIG. 3.—(*a*) Shell profiles of both baryon shell and dark matter shell at initial epoch $z = 200$ and at final epoch $z = 0$. The dark matter shell is about twice as thick as the baryonic shell at the final time. The short-dashed line is the analytic solution of a baryonic shell in the $\Omega = 1$, $\Omega_b \ll 1$ case (cf. Table 3 of Bertschinger 1985). The two vertical long-dashed lines indicate the position of the dark matter collisionless shell, the internal fine structures (cf. Fig. 3 of Bertschinger 1985). The oscillation of the density of the dark matter component is simply due to the discrete density assignment scheme that we employed, i.e., the CIC scheme. In the regions of dilute density, only a few particles are present, leading to inaccuracy of the CIC scheme. (*b*) Accuracy of the calculation over the whole run; the vertical coordinate is the ratio of computed total energy (gravitational energy plus kinetic and internal energy) to the analytic value, which is calculated by the cosmic energy equation (cf. eq. [33]). As the figure shows, accuracy of 2% is achieved. (*c*) Six parallel slices of the baryonic shell. (*d*) Six parallel slices of the dark matter shell. (*e*) One amplified slice of the baryonic shell. (*f*) One amplified slice of the dark matter shell. In (*c*)–(*f*), solid contours are $(1 + \sigma_b)^{i/2}$, and dotted contours are $(1 + \sigma_b)^{-i/2}$, where $i = 1, 2, 3$.

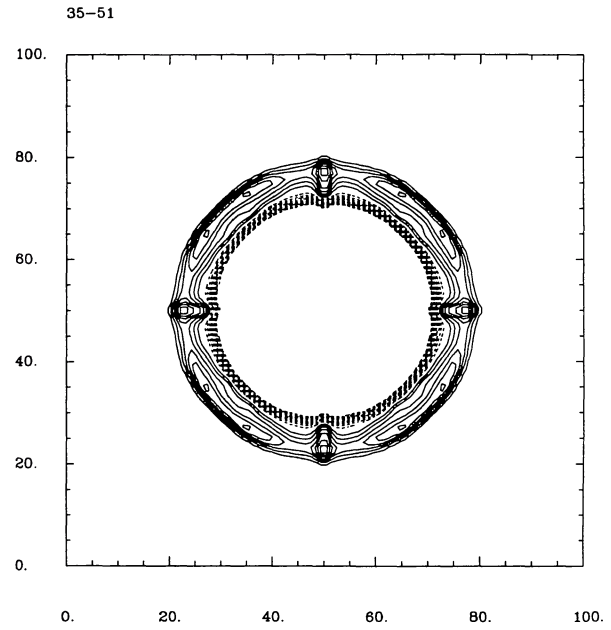

Baryonic Matter Density Contour of the Shell
solid contour: $(1+\sigma_b)^{1/2}$,
dotted contour: $(1+\sigma_b)^{-1/2}$, i=1,2,3,...

FIG. 3*e*

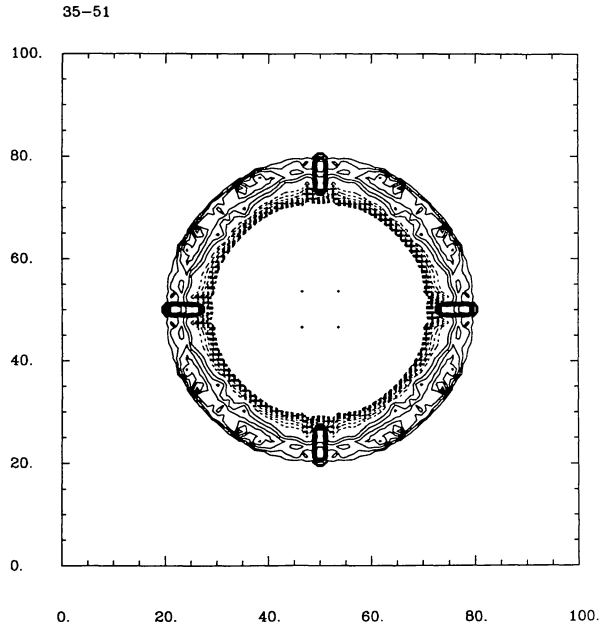

Dark Matter Density Contour of the Shell
solid contour: $(1+\sigma_b)^{1/2}$,
dotted contour: $(1+\sigma_b)^{-1/2}$, i=1,2,3,...

FIG. 3*f*

FIG. 3—*Continued*

temperature contours of the 64^3 run and the 128^3 run. They also show that the main structures did not change. This convinces us that numerical diffusions only affect shocked regions with a reasonably small smoothing length, and did not wash out interesting features. Figure 4*e* shows the density-density plot. The horizontal axis is the density of cells after being binned to 32^3 cells of the 64^3 run, and the vertical axis is the density of cells after being binned to 32^3 cells of the 128^3 run. The scattering around the solid line is due to the higher resolution in the 128^3 run, which in part is due to the inaccuracy of the FFT force calculation scheme; i.e., for the equation

$$\nabla^2\phi(\boldsymbol{x}) = \rho(\boldsymbol{x}) , \tag{78}$$

given $\rho(\boldsymbol{x})$, by FFT technique we can get $\phi(\boldsymbol{x})$; then by twice differencing $\phi(\boldsymbol{x})$ we get $\hat{\rho}(\boldsymbol{x})$, and thus the quantity ERR defined as

$$\mathrm{ERR} = \{4[(\hat{\rho}(\boldsymbol{x}) - \rho(\boldsymbol{x})]^2/[\hat{\rho}(\boldsymbol{x}) + \rho(\boldsymbol{x})]^2\}^{1/2} , \tag{79}$$

which we find to be 5%–10% on the cell scale for a typical cosmological density field.

TABLE 1

DENSITY FLUCTUATIONS AS A FUNCTION OF REDSHIFT

Fluctuation	$z = 10$	$z = 2$	$z = 0$
σ_M(fluid):128	0.328	1.568	4.319
σ_M(fluid):64	0.314	1.125	3.073
$\frac{\sigma_M(\text{fluid}):128}{\sigma_M(\text{fluid}):64}$	1.045	1.394	1.405
σ_M(dark):128	0.325	1.734	6.408
σ_M(dark):64	0.314	1.385	4.884
$\frac{\sigma_M(\text{dark}):128}{\sigma_M(\text{dark}):64}$	1.035	1.252	1.312

TABLE 2

DENSITY FLUCTUATIONS WITH DIFFERENT RESOLUTION

Fluctuation	128^3 Cells	64^3 Cells	32^3 Cells
σ_M(fluid)	2.209	1.977	1.519
σ_M(dark)	2.650	2.412	1.903
$\frac{\sigma_M(\text{fluid})}{\sigma_M(\text{dark})}$	0.834	0.820	0.798

This is the random error due to resolution, and we may be able to fit the dependence on resolution by the following formula:

$$\left(\frac{\Delta\rho}{\rho}\right)_{\text{rms}} = A\left(\frac{\Delta l}{l_{\text{bin}}}\right)_{\alpha}, \tag{80}$$

where Δl and l_{bin} are cell size and bin size in units such that the box size is 1; ρ is the average density of a cell from two runs, $\Delta\rho$ is the density difference of a cell between two runs, and A and α are two constants. We found that for the test considered, we use $(\Delta\rho/\rho)_{\text{rms}}$

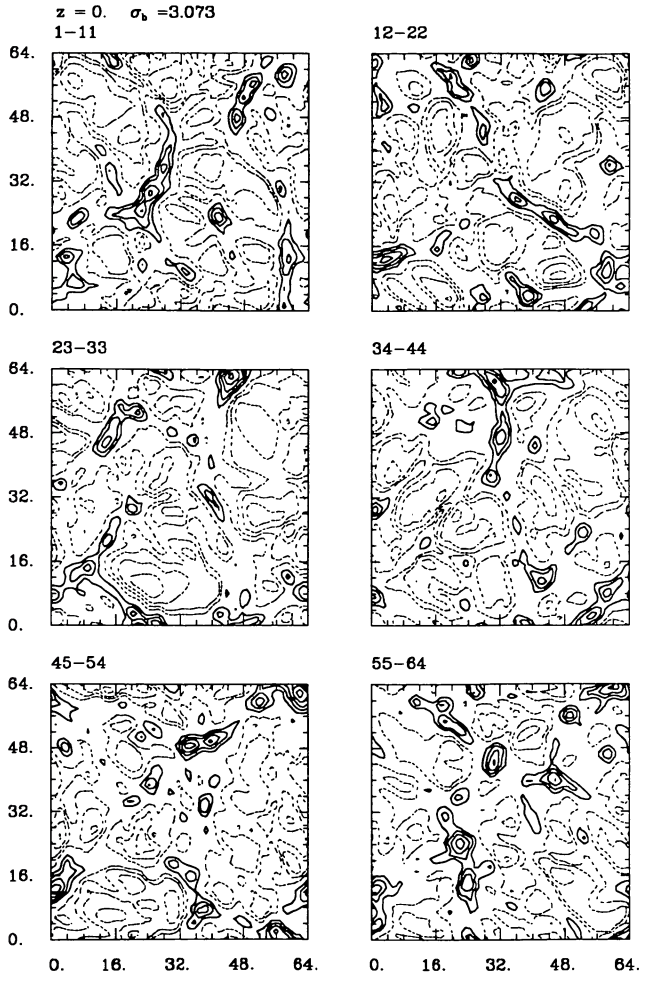

FIG. 4a

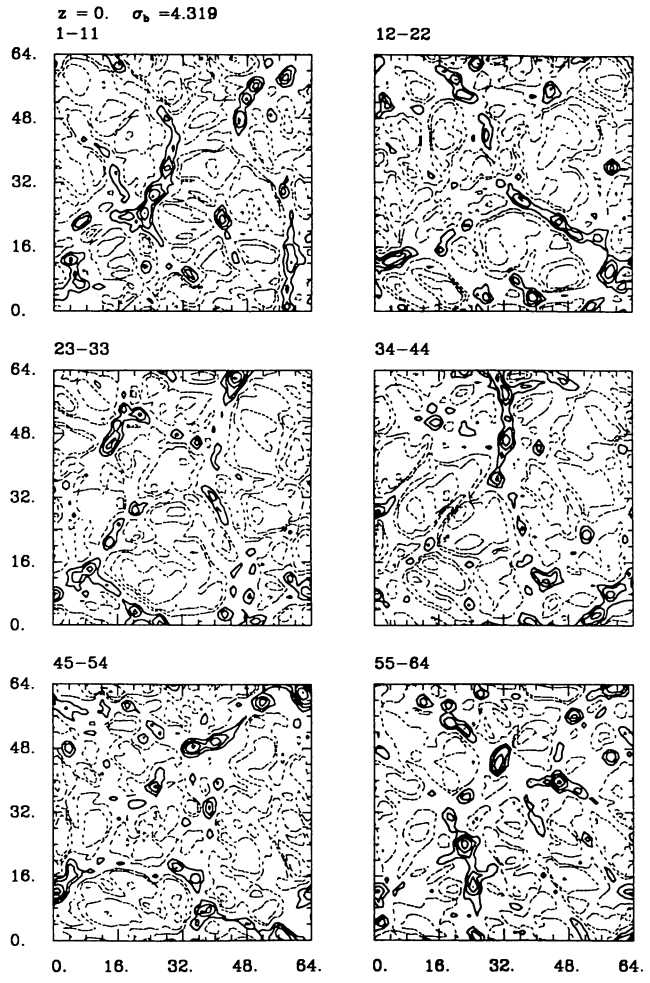

FIG. 4b

FIG. 4.—(*a*, *b*) Density contours of (*a*) the 64^3 run and (*b*) the 128^3 run at $z = 0$. They show that the main structure features remain the same, although there are more features which appear in the latter because of higher resolution. (*c*, *d*) Temperature contours of (*c*) the 64^3 run and (*d*) the 128^3 run at $z = 0$. They also show that the main structures did not change. (*e*) Density-density plot; the horizontal axis is the density of cells after being binned to 32^3 cells of the 64^3 run, and the vertical axis is the density of cells after being binned to 32^3 cells of the 128^3 run. In (*a*)–(*d*), $L = 64h^{-1}$ Mpc, $h = 0.5$, $b = 1.0$, $\Omega = 1.0$, $\Omega_b = 0.1$. Contours as in Fig. 3.

for $l_{bin} = 2$ and 4 cell sizes (cell of the 64^3 run) to determine A and α. We found that $A = 1.526$ and $\alpha = 0.140$ give a good fit, which is able to predict $(\Delta\rho/\rho)_{rms}$ for $l_{bin} = 8$ cell sizes with an accuracy of better than 1%. We see from Figure 4*e* that, as expected, in the 128^3 run binned to 32^3, the low-density regions are lower in density on average and the high-density regions higher on average than in the 64^3 run binned to 32^3. The higher resolution run is simply more accurate and better represents the tails of the density distribution at both ends.

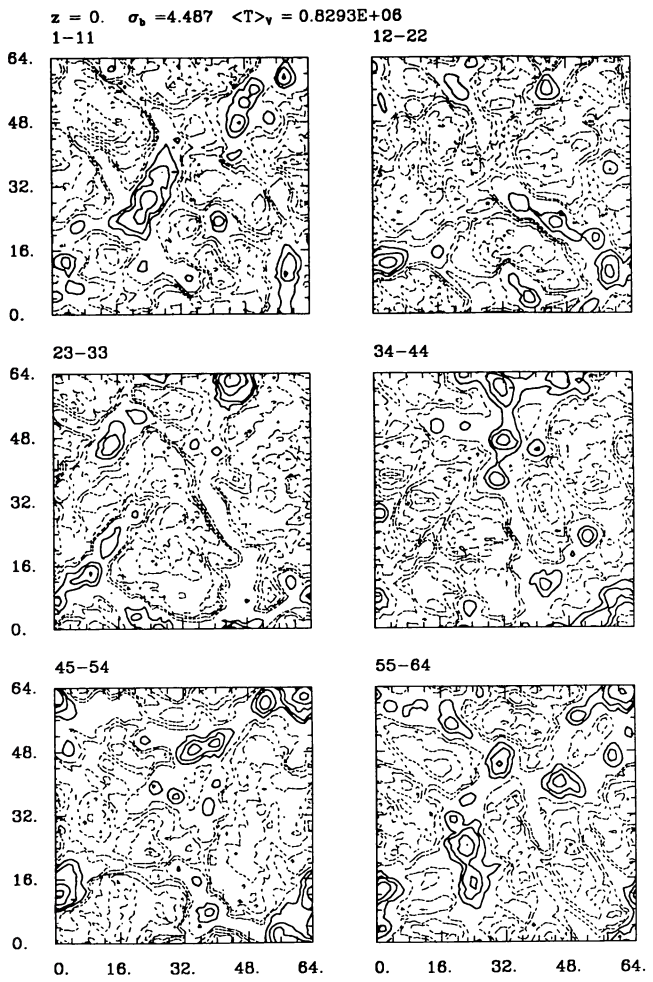

FIG. 4*c*

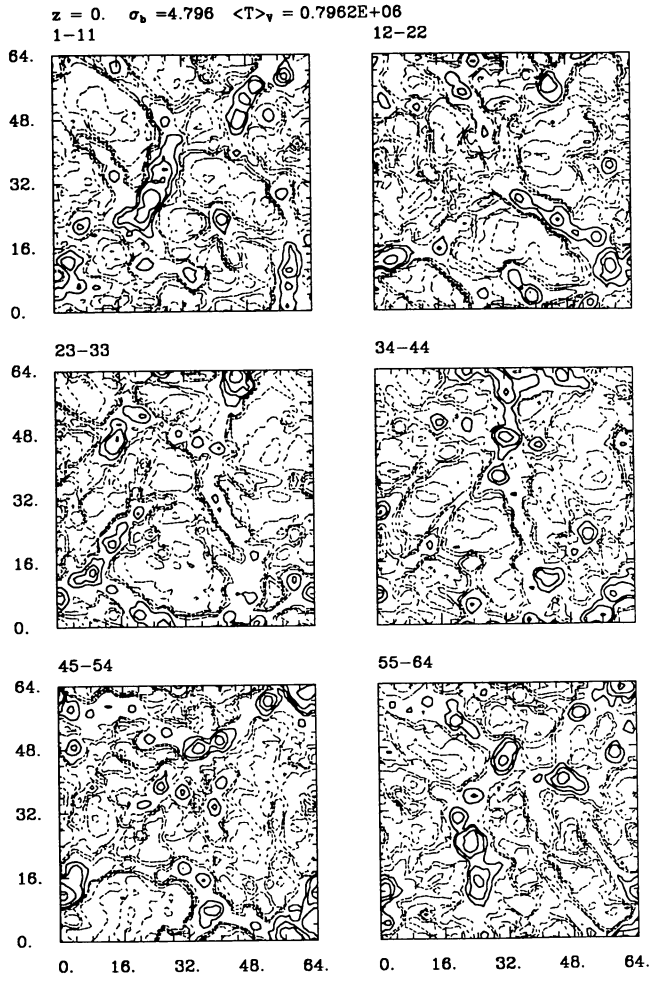

FIG. 4*d*

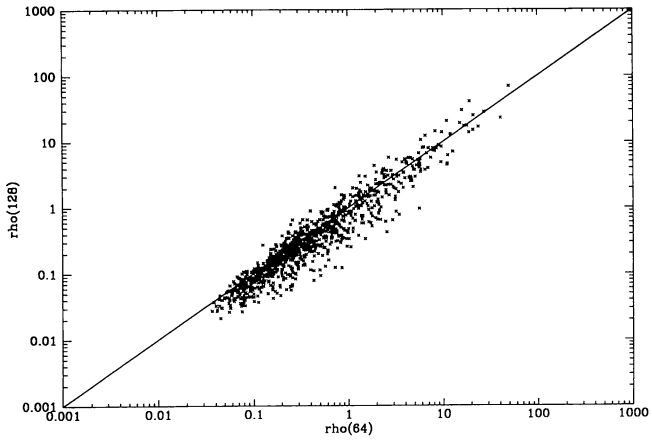

FIG. 4*e*

FIG. 4—*Continued*

5.7. *Experiments Testing the Effect of the Code on Some Integral Quantities due to Limited Resolution*

We made a set of experiments to test the effects on our final values of the Zel'dovich-Sunyaev y-parameter and the intensity of the X-ray background radiation field at frequency $\nu = 1$ keV due to the limited resolution as well as to the lower and upper cutoff of the power spectrum in a simulation. For any quantity w which is averaged over the whole simulated box, due to the limited resolution of the code, the computed result $\bar{w}_c$ should have some discrepancy from the true value which can be reached when the code has infinite resolution.

$$\bar{w}_c = \bar{w}_t - \delta w \,. \tag{81}$$

The discrepancy δw must depend on (1) the total simulated box size, $l_{\rm box}$, which we symbolize as $k_{\rm min}$, i.e., the lower bound of the input power spectrum; (2) the cutoff of the frequency at the high-frequency end of the input power spectrum, $k_{\rm max}$; (3) the cell size, $l_{\rm cell}$, for which we use the total number of cells on one side, N, instead. We can parameterize the error induced due to finite numerical resolution N, and a finite range of input waves $k_{\rm min} < k < k_{\rm max}$ as follows:

$$\delta w = (A + BN^{-\alpha})[e^{-\beta k_{\rm max}} + C(e^{\gamma k_{\rm min}} - 1)] \,. \tag{82}$$

To test our error estimation scheme, we made nine simulations using the BBKS CDM power spectrum with $h = 0.5$ and $b = 1.0$; they are listed in Table 3, where $k_{\rm min}$ and $k_{\rm max}$ are in units of h Mpc^{-1}, $\langle y \rangle$ ($z = 0$) is the computed mean Sunyaev-Zel'dovich parameter in units of 10^{-6} at $z = 0$, with indicated statistical error of the mean, as we sample a limited number of different computed lines of sight. The systematic error of our code is estimated by equations (81) and (82). In addition, $j(\nu = 1$ keV) is the computed intensity of the X-ray background radiation field at frequency $\nu = 1$ keV in units of 10^{-27} ergs cm^{-2} s^{-1} Hz^{-1} sr^{-1}. For $\langle y \rangle$ we found that if $A = 2.374 \times 10^{-6}$, $B = 2.0 \times 10^{-5}$, $C = 3.47$, $\alpha = 0.28$, $\beta = 0.34$, and $\gamma = 1.67$, we have a fairly good fit of the nine runs, which gives the extrapolated value of the $\langle y \rangle$ parameter 1.25×10^{-5}. Consider our most accurate run, No. 2, with $128^3 = 2 \times 10^6$ dark matter particles and cells and waves ranging from 128 to 2 Mpc permitted in our initial conditions. Then we find that $\langle y \rangle = 6.0 \times 10^{-6}$. Extrapolating this to a numerically perfect calculation ($N \rightarrow \infty$) with the same input spectrum, we have $\langle y \rangle = 8.28 \times 10^{-6}$, an increase of 38%. Our fitting tells us that this value is 66% of the true value, with an additional contribution of 31% arising from waves with $\lambda < 2$ Mpc, and 3% with waves of $\lambda > 128$ Mpc. Similar extrapolations can be made for other quantities if they are of an integral or average nature. It is difficult to estimate the accuracy of this extrapolation without further extensive calculations, except to say that the final, extrapolated result $\langle y \rangle = 1.25 \times 10^{-5}$ has an error of less than the difference between it and the best single run, i.e., $\langle y \rangle = (12.5 \pm 6.5) \times 10^{-6}$ should present a conservative estimate of final accuracy. We did the same fitting procedure for the X-ray intensity $j(\nu = 1$ keV), and we found that with $A = 21.1$, $B = 118.4$, $C = 2.39$, $\alpha = 0.64$, $\beta = 0.95$, and $\gamma = 1.13$, we have a fairly good fit of the nine runs, which gives the extrapolated value of $j(\nu = 1 \text{ keV}) = (27.16 \pm 17.16) \times 10^{-27}$ ergs cm^{-2} s^{-1} Hz^{-1} sr^{-1}, which at the lower limit is consistent with the value of the best run and at the upper limit is about a factor of 4.5 times that, and on average is about 3 times that of the best single run.

5.8. *Comparison between the Computed Background Radiation Field $i(\nu)$ and the Analytic Calculation*

We made the comparison between the final computed X-ray radiation field and that of the analytic calculation (cf. Loeb & Ostriker 1991) using the average evolutionary values of density fluctuations and temperatures in the same run. The agreement is very good, but the spectrum of the analytic calculation drops off faster at the high-energy end, which is mainly because of the non-Gaussian property of the density and temperature distributions in the real simulation.

6. CONCLUSION

If we had a perfect, infinitely powerful computer, our hydrodynamic code will work perfectly. But because of the limited power of present computers, our code suffers some unavoidable errors due to various approximations being made in the process of trans-

TABLE 3

NUMERICAL EFFECTS OF THE CODE

Run	N	$k_{\rm min}$	$k_{\rm max}$	$\langle y \rangle (z = 0)$	$j(\nu = 1 \text{ keV})(z = 0)$
1	64	1/64	1/2	4.1 ± 0.19	5.99
2	128	1/64	1/2	6.0 ± 0.15	10.0
3	64	1/64	1/4	3.7 ± 0.18	1.97
4	32	1/64	1/4	1.2 ± 0.16	0.40
5	32	1/32	1/2	2.1 ± 0.11	0.56
6	32	1/32	1/4	1.3 ± 0.07	0.30
7	16	1/32	1/4	0.6 ± 0.03	3.07×10^{-6}
8	16	1/32	1/8	0.33 ± 0.07	3.07×10^{-6}
9	16	1/16	1/2	$0.7 \times 10^{-6} \pm 0.1 \times 10^{-6}$	0.37×10^{-6}

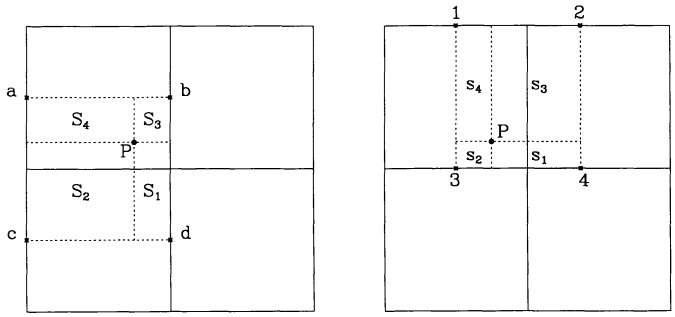

FIG. 5.—CIC interpolating scheme in the two-dimensional case. In the three-dimensional case the weights are volumes instead of areas.

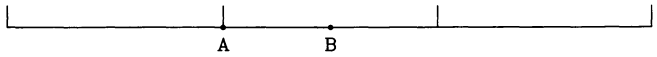

FIG. 6.—Error due to the assignments of particle quantities to the grids in the CIC scheme.

forming a set of analytic physical equations into a set of numerically approximate equations and to finite time steps. Since we cannot have infinitely small cell size while having an infinitely big box size, the dynamic range is severely limited. Fortunately, the present available computer resources just begin to make it meaningful for us to follow numerically the three-dimensional evolution of the universe. The available scenarios of cosmological models allow us to compute the most interesting quantities of the large-scale structure without the necessity of excluding main features of the given initial conditions. In order to compute the physical quantities in a reasonably accurate way, we need to include most of the energy of the power spectrum while reaching the proper small scales where energy dissipation and shock heating are maximum. Take the CDM scenario as an example: the energy peak of the power spectrum lies about the wavelength of $50h^{-1}$ Mpc for $h = 0.5$, and the maximum shock heating happens at the scale of about $0.3h^{-1}$ Mpc, so we need about 200^3 cells to include about 90% of the total energy while still including small enough scales to compute the effects of shocks. The largest runs we have made are 128^3, which is still a factor of 4 short of what we have described as necessary. After some extensive tests, we found that we could split the whole relevant scales into several subregions which overlap each other to some extent. Using this approach, we are able to compute with reasonable computer time and memory usage.

The tests described above tell us that the hydrodynamic code is accurate and robust, and the effects due to numerical diffusion can be predicted to some extent, and can be reduced from the final output. It can capture a fairly clean shock within 3–4 cells; the overall quantities have an integrated accuracy of about 1%–3%; numerical diffusion only affects shock regions, and overall effects on computed physical quantities due to numerical diffusion are small. We are confident that our numerical results are sound, and features in our results averaged over several cells should not be affected by the numerical diffusion significantly.

The code is well organized and structured; it is ready to have new features added into it. Some of the next interesting physical processes which can be added are the following:

1. The relaxation time between electrons and protons is an inverse quadratic function of density; some preliminary calculations show that only very high density regions are completely relaxed, i.e., electrons and protons have the same temperature (cf. Zel'dovich & Raizer 1966). On the other hand, in less dense regions, after matters have been shocked, the protons get most of the heat energy because of their high inertial mass compared with electrons, so the proton temperature will be higher than the electron temperature. Then there must be energy transfer between electrons and protons because of the different temperatures. Besides, all the cooling processes in these less dense regions will be lowered considerably, leading to further deleting of mass in the least dense regions, making collapse of moderate dense regions more difficult. Additionally, since the Compton effect cools only the electrons, the ions will act as a storage battery to reheat the electrons at later epochs.

2. The second important physical process to add is probably the transfer of the radiation equation, which basically has the effect that radiation from dense high-temperature regions will be absorbed on the spot before these regions become optically thin at the hydrogen Lyman limit, and also at the two helium ionization peaks due to He I and He II. So while these regions remain optically thick, the less dense and lower temperature regions will see no ionizing radiation. They will remain highly neutral because collisional ionization is unimportant in these regions. On the other hand, radiating regions have more photons to get ionized. However, our calculations, without including this effect, already show that the mass-weighted neutral fractions of both hydrogen and helium are higher than volume-weighted ones, i.e., high-density regions are more ionized than lower density regions. But this could in part be due to higher collisional ionization rates in high-density regions. We think that this process will have the following effect: the dense regions will have less cooling and collapse less easily; less dense regions will stay at higher temperatures, too, although whether the final radiation field will be higher or lower is not clear, but the Zel'dovich-Sunyaev effect will be reduced a bit.

3. The third thing to add is another component, i.e., baryonic particles due to collapsed objects, which could be stars, star globular clusters, galaxies, or maybe even dense clusters of galaxies. Meanwhile, there will be certain energy feedback during certain periods of time in various forms, such as galactic winds, quasars, even the collective radiation from stars or globular clusters, which will ionize the baryonic intergalactic or intercluster medium significantly in early times. The principles behind this are presented in

the papers of Rees (1985) with respect to ionization and Ikeuchi & Ostriker (1986) and their colleagues, with respect to shock heating. Obviously, the addition of this component will require mechanisms for the formation of these objects (cf. Baron & White 1987; Katz 1991).

4. Another process to add is the conduction process: it is important when free electrons exist and magnetic fields are not strong. It is especially relevant when there is a significant temperature gradient. It will reduce temperatures of high-temperature zones while getting nearby low-temperature zones heated up. To some extent our diffusive code already has included some part of thermal conduction. Conduction is a process which conserves internal energy, so the mean effect of the Zel'dovich-Sunyaev effect is not likely to change significantly, though it will change slightly because there are high-order processes involved, e.g., change of temperature of a zone will change radiative cooling processes, and so on. However, it is likely that there may be a relatively bigger change in the fluctuations of the Zel'dovich-Sunyaev effect; whether reducing or increasing it is not obvious, but most likely it will be reduced.

I am pleased to acknowledge always valuable and inspiring advice and persistent guidance from my thesis adviser, J. P. Ostriker, and financial support from NASA grant NAGW-765. The work would not have been possible had not A. Jameson made his highly developed aerodynamics code available for astrophysical applications. I would like to thank A. Jameson for letting me use his Convex 210 computer, and also to thank D. H. Weinberg for making his various valuable codes available to me and for his helpful discussions. The many discussions with J. Binney, B. T. Draine, G. Evrard, J. E. Gunn, J. Goodman, A. Loeb, G. Miralda, C. Park, and M. Strauss were also very helpful. I would like to thank I. Renda for carefully checking the English in the paper. And, finally, I would like to thank an anonymous referee for a careful reading of the manuscript leading to a number of corrections and clarifications.

REFERENCES

Aarseth, S. J. 1971, Ap&SS, 13, 324
———. 1974, A&A, 35, 237
Acton, F. S. 1970, Numerical Methods That Work (New York: Harper & Row)
Bardeen, J. M., Bond, J. R., Kaiser, N., & Szalay, A. S. 1986, ApJ, 304, 15 (BBKS)
Baron, E., & White, S. D. M. 1987, ApJ, 322, 585
Bertschinger, E. 1985, ApJS, 58, 1
Binney, J. 1977, ApJ, 215, 483
———. 1990, private communication
Black, J. H. 1981, MNRAS, 197, 553
Blaes, O. M., Goldreich, P. M., & Villumsen, J. V. 1990, ApJ, 361, 331
Bond, J. R., Centrella, J., Szalay, A. S., & Wilson, J. R. 1984, MNRAS, 210, 515
Bouchet, F. R., & Hernquist, L. 1988, ApJS, 68, 521
Broadhurst, T. J., Ellis, R. S., Koo, D. C., & Szalay, A. S. 1990, Nature, 343, 726
Carlberg, R. G., & Couchman, H. M. P. 1989, ApJ, 340, 47
Carlitz, R., Frautschi, S., & Nahm, W. 1973, A&A, 26, 171
Cen, R. Y., Jameson, A., Liu, F., & Ostriker, J. P. 1990, ApJ, 362, L41
Chiang, W. H., Ryu, D., & Vishniac, E. T. 1989, ApJ, 339, 603
Davis, M., & Peebles, P. J. E. 1983, ApJ, 267, 465
Dekel, A., & Rees, M. J. 1987, Nature, 330, 455
Efstathiou, G., Davis, M., Frenk, C. S., & White, S. D. M. 1985, ApJS, 57, 241
Evrard, A. E. 1988, MNRAS, 235, 911
Gunn, J. E., & Peterson, B. A. 1965, ApJ, 142, 1633
Hernquist, L., & Katz, N. 1989, ApJS, 70, 419
Hogan, C. J. 1989, ApJ, 340, 1
Hwang, J. C., Vishniac, E. T., & Shapiro, P. R. 1989, ApJ, 346, 12
Ikeuchi, S. 1981, PASJ, 33, 211
Ikeuchi, S., & Ostriker, J. P. 1986, ApJ, 301, 522
Jameson, A. 1989, Science, 245, 361
———. 1988, in IAU Symp. 130, Large Scale Structure of the Universe, ed. J. Audouze, M-C Pelletan, & A. Szalay (Dordrecht: Reidel), 43
Katz, N. 1991, ApJ, 368, 325
Loeb, A., & Ostriker, J. P. 1991, Nature, preprint
McGill, C. 1990, MNRAS, 242, 544
Melott, A. L., & Fry, J. N. 1986, ApJ, 305, 1
Muchet, J. P., Haubold, H. J., Nuller, V., Gottlober, S., & Mathai, A. M. 1988, A&A, 203, 211
Osterbrock, D. E. 1989, Astrophysics of Gaseous Nebulae and Active Galactic Nuclei (Lick Observatory, University of California Santa Cruz)
Ostriker, J. P., & Cowie, L. L. 1981, ApJ, 243, L127
Park, C. B. 1990, MNRAS, 242, 59P
Peebles, P. J. E. 1971, Physical Cosmology (Princeton: Princeton Univ. Press)
———. 1980, The Large-Scale Structure of the Universe (Princeton: Princeton Univ. Press)
Press, W. H., Flannery, B. P., Teukolsky, S. A., & Vetterling, W. T. 1986, Numerical Recipes (Cambridge: Cambridge Univ. Press)
Press, W. H., & Schechter, P. 1974, ApJ, 187, 425
Rees, M. J. 1985, MNRAS, 213, 75P
———. 1988, in IAU Symp. 130, Large Scale Structure of the Universe, ed. J. Audouze, M-C Pelletan, & A. Szalay (Dordrecht: Reidel), 437
Rees, M. J., & Ostriker, J. P. 1977, MNRAS, 179, 541
Richtmyer, R. D. 1957, Difference Method for Initial-Value Problems (New York: New York Univ. Press)
Rybicki, G. B., & Lightman, A. P. 1979, Radiative Processes in Astrophysics (New York: Wiley)
Ryu, D., Vishniac, E. T., & Chiang, W. H. 1990, ApJ, 354, 389
Sargent, W. L. W., Young, P., & Schneider, D. P. 1982, ApJ, 256, 374
Schwarz, J., Ostriker, J. P., & Yahil, A. 1975, ApJ, 202, 1
Shapiro, P. R., & Struck-Marcell, C. 1985, ApJS, 57, 205
Silk, J. 1977, ApJ, 211, 638
Sod, G. A. 1978, J. Comput. Phys., 27, 1
Spitzer, L., Jr. 1978, Physical Processes in the Interstellar Medium (New York: Wiley)
Sunyaev, R. A., & Zel'dovich, Ya. B. 1970, Ap&SS, 7, 13
Tully, R. B. 1982, ApJ, 257, 389
von Neumann, J., & Richtmyer, R. D. 1950, J. Appl. Phys., 21, 232
Weinberg, D. H. 1990, Ph.D. thesis, Princeton Univ.
Weinberg, D. H., & Gunn, J. E. 1990, MNRAS, 247, 260
Weinberg, D. H., et al. 1991, in preparation
White, S. D. M., Davis, M., Efstathiou, G., & Frenk, C. S. 1987a, Nature, 330, 451
White, S. D. M., Frenk, C. S., Davis, M., & Efstathiou, G. 1987b, ApJ, 313, 505
White, S. D. M., & Ostriker, J. P. 1990, ApJ, 349, 22
White, S. D. M. 1988, in NATO Advanced Study Institute on the Early Universe, ed. W. G. Unruh & G. W. Semenoff (Dordrecht: Reidel), 239
Young, P., Sargent, W. L. W., Boksenberg, A., & Oke, J. B. 1981, ApJ, 249, 415
Zel'dovich, Ya. B. 1970, A&A, 5, 84
Zel'dovich, Ya. B., & Raizer, Yu. P. 1966, Physics of Shock Waves and High Temperature Hydrodynamic Phenomena, Vol. 2
Zel'dovich, Ya. B., & Sunyaev, R. A. 1969, Ap&SS, 4, 301